POLITECNICO DI MILANO
Master of science in Geoinformatics Engineering
Dipartimento di Ingegneria Civile a Ambientale,
Dipartimento di Elettronica, Informazione e Bioingegneria.

SAR-BASED COASTLINE DETECTION AND MONITORING

Supervisor: Prof. Giovanna Venuti
Co-supervisor: Ing. Marco Manzoni

Thesis by:
Marco Mazzolini
Student ID: 914117

Academic year 2020-2021

A mio padre..

Contents

Abstract

Natural events and human activities can significantly change our planet. The coastal environment is among the most fragile ones, its efficient monitoring is crucial to manage properly human and natural resources located in this environment where a large portion of our population lives. This thesis aims at exploring the capabilities of Synthetic Aperture Radar (SAR) for coastline detection and monitoring. This technology is chosen over optical systems because of the maturity reached with the launch of the Sentinel-1 mission and because SAR systems can operate day-and-night time and all-weather. Moreover, water has a distinctive behavior in SAR images.
After a state-of-the-art analysis of available techniques, this thesis proposes two novel approaches for shoreline detection and coastal monitoring.

The iterative detection method is based on the SLIC algorithm and segments the imagery in units that are then filtered and classified as water or land with a thresholding technique. The goal is to fit accurately the image features to preserve the coastline details. Results of the algorithm are compared to a manually-detected shoreline for the Lizard Island case study.

The coastline monitoring approach exploits a long time-series of SAR acquisitions to describe the modifications of the coast. The preprocessing involves a season-wise temporal averaging to erase tidal effects. However, the major innovation is the introduction of a land-water index that allows for the comparison between acquisitions with a different sea state, which would negatively influence the analysis. The proposed index is modeled in time on a pixel basis. A visualization technique that exploits the HSV codification of the color space highlights where and when changes happened. A case study for this technique is carried out over the Reentrâncias Maranhenses, where results are qualitatively assessed by comparisons with optical data and with the output of an existing (deep learning) approach.

Sommario

Eventi naturali ed attività umane possono modificare profondamente l'ambiente costiero. Monitorare in maniera efficiente queste zone, in cui vive una grande fetta della popolazione, è importante per la corretta gestione delle risorse. L'obiettivo di questa tesi è di investigare le possibilità del Radar ad apertura sintetica (SAR) per l'identificazione ed il monitoraggio della linea di costa. Questa tecnologia è stata scelta in virtù del grado di maturità raggiunto con la missione europea Sentinel-1. Il SAR viene preferito ai sistemi ottici in quanto ha la capacità di operare giorno e notte ed in qualsiasi condizione meteo, inoltre l'acqua è facilmente riconoscibile in questo tipo di immagini. Dopo avere analizzato lo stato dell'arte, in questa tesi vengono proposti due nuovi algoritmi per l'individuazione della linea di costa e per il suo monitoraggio.

L'algoritmo di individuazione della linea di costa è basato sulla segmentazione dell'immagine con SLIC in unità chiamate superpixels che vengono poi filtrate ed in seguito classificate come appartenenti alle classi acqua e terra. L'idea è che utilizzare i superpixel come prima operazione possa preservare il dettaglio della linea costiera. La validazione consiste nel confronto del risultato con una costa individuata manualmente nell'isola di Lizard.

Il monitoraggio sfrutta una lunga serie temporale di acquisizioni SAR per descrivere lo spostamento della linea di costa. L'effetto delle maree viene annullato grazie ad una media stagionale, ma l'innovazione più rilevante è l'introduzione di un indice che permette di annullare l'oscillazione caratteristica dei pixel di acqua, causata dal variare del moto ondoso. L'andamento temporale dell'indice proposto viene modellizzato tramite una regressione lineare. La posizione e l'istante dei cambiamenti alla linea di costa sono espressi con una visualizzazione ad-hoc. Una validazione qualitativa è eseguita confrontando i risultati con immagini ottiche e con un algoritmo esistente (deep learning) nella riserva naturale delle Reentrâncias Maranhenses.

Chapter 1

Introduction

1.1 The problem

A coast is the highly dynamical area that defines the boundary between land and water, be it an ocean, a sea, or a lake [Turner et al., 1998]. This region hosts crucial infrastructures, ecosystems, and about 40% of the world's global human population [Martinez et al., 2007]. Monitoring and managing the coastal areas are tasks of considerable social and economic importance. The coastline (or shoreline) can be defined as the physical interface between land and water [Dolan et al., 1991]. A stable shoreline naturally presents an oscillation due to the tidal variation of the sea level. This makes single epoch monitoring possibly misleading.

However, our coasts undergo constant changes as rivers, nearshore currents, and waves move sediments inside, outside, and within the nearshore zone. Morphological evolution tends to accelerate under events, such as storms and tropical cyclones. These extremes drive intense erosion and can lead to irreversible changes. The human presence is also a strong footprint driver. Planned exploitation of coastal resources and side effects of other activities result in the deterioration of the litoral environment. Moreover, global warming induces ice melting that causes sea-level rise. The latter contributes to coastal erosion, especially in low-lying and flat areas, through a complex morphological adaptation [Mentaschi et al., 2018]. Furthermore, shoreline erosion and coastal flooding are among the gravest effects of climate change according to the Intergovernmental Panel on Climate Change (IPCC) [IPCC, 1990].

Having up-to-date information about the coastal dynamic is crucial for

proper coastal management. For example, it would be an error to nourish a beach in an accretion phase [Stive et al., 2002]. Many in-situ methods for shore(line) monitoring have been used, such as direct measuring of distances [Ferreira et al., 2006] and monitoring with laser, cameras, aerial photogrammetry. This kind of high-resolution data helps in the understanding of the coastal dynamic. However, the drawbacks are the highly local nature of the monitoring and the consistent costs (in terms of labor and equipment) if the goal is wide-area monitoring.

Satellite remote sensing (RS), thanks to the availability of big data facilities dedicated to storage and elaboration [Gorelick et al., 2017] is a resource for coastline monitoring. Optical RS, because of its high resolution has been and is widely used for coastline extraction and monitoring [Garcia-Rubio et al., 2015], [Mentaschi et al., 2018], [Teodoro, 2016], [Toure et al., 2019]. Nevertheless, crucial drawbacks are cloud impenetrability in the visible part of the spectrum and lack of illumination during the night. These issues reduce the availability of imagery for consistent and systematic monitoring. For example, clouds can obscure a coastline area for many subsequent satellite passes, and data-holes would become systematic in bad-weather seasons. In synthesis, the problems that this thesis aims to solve are:

1. to detect the coastline with a precise and authomatic algorithm;
2. to monitor the coastal modifications in time (a consistent data source is needed).

1.2 The solution

Synthetic aperture radar (SAR) is an attractive alternative for the problem under study. Satellite-based SAR overcomes the drawbacks listed for optical RS. Since it is an active sensor, it is not affected by sunlight absence. Moreover, its signal is in the microwave part of the spectrum and can penetrate the water droplets that form clouds. Hence SAR is nearly all-weather. Moreover, revisit interval and coverage of many SAR missions are suitable for coastline monitoring.

For the purpose of this thesis, it is possible to describe SAR as an instrument that maps the roughness of the earth's surface. Water bodies have a characteristic low response because of their relative flatness with respect to the ground. Moreover, the consistency of acquisitions permits time averaging with the median operator. This enables the individuation of the average coastline over a certain period.

The observation of SAR systems is a complex number which depend on amplitude and phase of the back-scattered signal. The solution here proposed exploits just the amplitude information of SAR images. However, speckle is a distinctive feature of SAR imagery and can cause disturbances to coastline recognition. It is caused by constructive/destructive interference of back-scattered electromagnetic waves.

This thesis proposes a new iterative detection method based on scene segmentation. The image is divided into groups of uniform pixels, called superpixels. The main idea behind the new approach is to use the ability of superpixels to follow the image features and obtain a homogeneous region (with a common covering: land or water) to filter the speckle and preserve the spatial resolution. The partition between land and water superpixels is done by exploiting the classic thresholding algorithm Otsu's method and the machine learning approach of Gaussian mixtures.

For the monitoring, the main issue is caused by the wave modification of water backscattering. This work introduces a Normalized Land-Water Index (NLWI), which maps a pixel backscattering into the similarity to the land or water classes, by erasing the wave disturbance. This index's goal is a consistent comparison of backscattering in time. It is possible to model this index's variation in time to detect the change in land cover and estimate the change-date. In the validation, we found that linear regression is a suitable option. Finally, an interesting visualization of the change in land covering date is introduced.

1.3 Thesis outline

In chapter 2, a common theoretical basis is laid out. The main features of SAR systems are explained, and the amplitude image is characterized. This will be limited to the useful concepts for the solution of the problem tackled in the thesis. Moreover, the main SAR missions relevant to this problem are described.

In chapter 3, a state of the art analysis for coastline detection and monitoring is carried out. Additionally, the superpixel concept is explained and, the novel method for coastline detection adopting superpixels is described in detail. Finally, a coastline changes visualization technique is introduced.

In chapter 4, the Google Earth Engine platform, that is used for data exploration and acquisition, is described. In addition, the case studies are described and used to test and validate the methods described in the previous chapter.

In chapter 5, the conclusions of the work are drawn. Possible improvements are suggested.

Chapter 2

Theoretical background

In 1978 the first space-borne SAR mission named SEASAT was launched. It was just the first of many. Fifty years later more than 25 satellite-based SAR systems are operating, of which 10 launched in the last five years. We can say this technology is in its full maturity [Moreira et al., 2013]. This chapter aims to give the reader a fast overview of the SAR geometry and working principles, the target types, the pixel brightness, and an intuitive definition of speckle. Later, two relevant missions for the research problem are described in their most distinctive features.

2.1 SAR basics

A SAR system is a radar system with a side-looking radar installed on a platform with a forward movement, as Figure 2.1 shows. The satellite or airplane flight path simulates a large antenna aperture. The synthetic antenna overcomes the problem of low azimuth resolution, which was present in the side-looking aperture radar (SLAR) that was the classic radar imaging system until the '50s [Moreira et al., 2013].

The geometry is side-looking since it measures the total transmission, reflection, and reception time of the signal through coherent detection. The measured interval locates the cell. A nadir-looking system would present right/left ambiguities. The frequency band can vary from 0.25-0.5 GHz, for the P band, to 26-40 GHz for the K_a band. The corresponding wavelengths range from 1 m to less than 1 cm. However, this parameter is fixed and decided in the mission design process. Media penetration of the electromagnetic pulses increases for radar systems using longer wavelengths. The polarization is the direction of oscillation of the emitted or received electro-

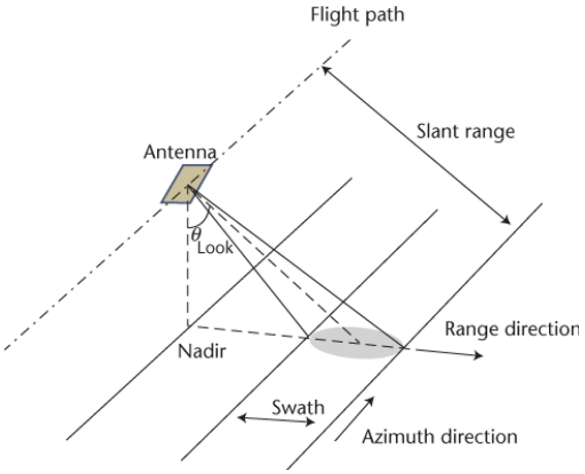

Figure 2.1: The side-looking geometry of SAR-systems.

magnetic wave. There are four possible configurations:

1. VV: an electromagnetic wave is transmitted vertically polarized and the receiver is configured to receive just the vertical polarization;

2. VH: an electromagnetic wave is transmitted vertically polarized and the receiver is configured to receive just the horizontal polarization;

3. HV: an electromagnetic wave is transmitted horizontally polarized and the receiver is configured to receive just the vertical polarization;

4. HH: an electromagnetic wave is transmitted horizontally polarized and the receiver is configured to receive just the horizontally polarization.

SAR polarimetry studies the behavior of terrain with respect to the different configurations that form the polarimetric scattering matrix. It can be used to estimate qualitative and quantitative physical information about land, snow, ice, ocean, and urban surfaces.

2.2 Target characteristics

SAR signal interacts with earth's surface and only a portion is scattered back to the platform. The capability of a target to reflect the electromagnetic wave in the direction of the platform is measured with a quantity called Radar Cross Section (RCS). Different surface features can be derived by looking just at the amplitude of the received (backscattered) signal. This thesis approach is centered on the backscattered amplitude that is addressed as

backscattering in the rest of the document. The system design provides a resolution cell with a size of several to hundreds of square meters, while the wavelength of the signal is several orders of magnitude smaller. Hence, multiple targets that interact independently with the signal are present in the same cell. It is necessary to distinguish between two types: point target and distributed target.

2.2.1 Point target

A point target is an object that makes all the backscattered signal come from a single point. A radar reflector belongs to this kind of target and is used to calibrate SAR systems. However, also a mirror with the right orientation can be a point target. When dealing with coastal imagery, urban areas can contain buildings with a particular double or triple bounce scattering mechanism. This strong signal dominates the return of the resolution cell.

2.2.2 Distributed target and speckle

More commonly, many elementary scatterers are in the same resolution cell. As the wave interacts with the targets, each element contributes to the backscattered wave with a phase and amplitude change. Figure 2.2 depicts this phenomenon. Single contributions are not observable, as the system measures the received signal altogether (the red vector).

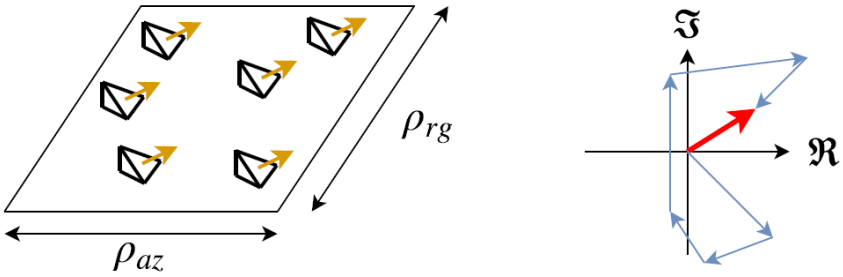

Figure 2.2: On the left: a distributed target that contains multiple elementary scatterers. On the right: the complex return is the superposition of all the contributions coming from the different scatterers.

The observed signal is affected by interference effects because of the phase differences between scatterers. Speckle can be understood as an interference phenomenon in which the principal source of the *noise-like* quality of the observed data is the distribution of the phase terms. Figure 2.3 is an example of this phenomenon. There is high variability in backscattering inside

homogeneous patches representing the fields. The result is a grainy image, which makes it hard to interpret the main features of the surface imaged by the SAR. Speckle resembles a salt-and-pepper effect.

Figure 2.3: An example of speckle: the SAR scene was acquired on 21/4/1994 over Tiber Valley. It shows some agricultural fields, note the intensity variation in the homogeneous patches.

The amplitude of a resolution cell can be modeled as a Rayleigh random variable [Oliver and Quegan, 1998]. Independent measurements of the same target can be averaged to smooth out the speckle. The independence is obtained by splitting the synthetic aperture into smaller sub-apertures, the so-called "looks", each separately processed and then averaged. When the needed smoothing of the speckle is even higher the radiometric resolution can be improved with moving window filters. This operation changes the intensity of the central pixel depending on the intensities of all the pixels within the window. In conclusion, speckle is reduced at the expense of spatial resolution.

2.2.3 Pixel brightness

The signal return depends on surface roughness and the nature of the material. The first depends on the relative size of the surface texture and the system wavelength, as Figure 2.4 depicts. If the surface roughness of the material is smooth, the radar beam is reflected according to the law of reflection. This phenomenon is a specular reflection. On the other end,

the radar beam is scattered in all directions for objects with a texture size comparable to the signal's wavelength. This phenomenon is called diffuse reflection and happens because of the multiple interactions. Variations in the surface roughness result in variations in the amount of diffuse scattering and varying pixel brightness.

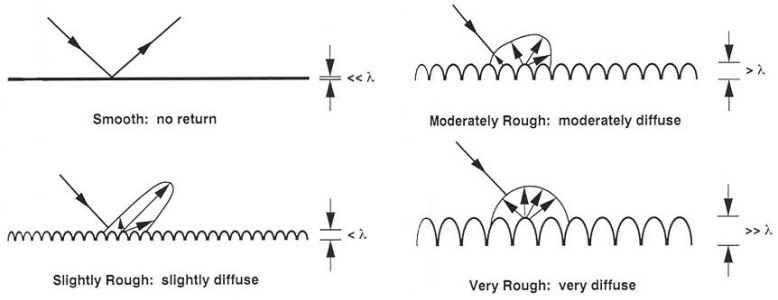

Figure 2.4: Surface roughness influences the reflection mechanism of the incoming signal depending on the relative size of the wavelength and surface texture.

Moreover, the scattering material influences the backscattering depending on its dielectric constant, which is a physical property of a material that determines how reflective that material is to electromagnetic waves. Metallic objects and water have a higher dielectric constant and are more reflective. However, since they are smooth with respect to the system wavelength and usually flat, the radar beam is specularly reflected away from the sensor.

2.2.4 SAR strengths

As we stated in the introduction, SAR systems overcome many drawbacks that are intrinsic in optical RS. First, radar systems are in the category of active remote sensing. Active systems can emit an electromagnetic wave that illuminates the target constantly and measure the backscattered signal after the interaction with the sensed object. On the other end, passive RS relies on an external illumination source, like the sun or the radiation from the object itself. Hence, source obscuration leads to disruptive interruption of the service. For example, an optical sensor cannot gain information related to the coast position during the night.

Secondly, SAR operational frequencies are designed to travel from the platform to the earth's surface with the weakest interaction with the atmosphere. As Figure 2.5 shows, the atmosphere is completely transparent for a signal in the so-called "radio window". Also, the optical systems can see through the atmosphere. However, this Figure refers to atmospheric gaseous

composition. Another common element in the atmosphere is liquid-phase water. When it gathers in large numbers of tiny droplets it forms a cloud. As every human knows, clouds are not transparent. For optical satellites, it is the same: clouds can obscure the vision of earth's surface.

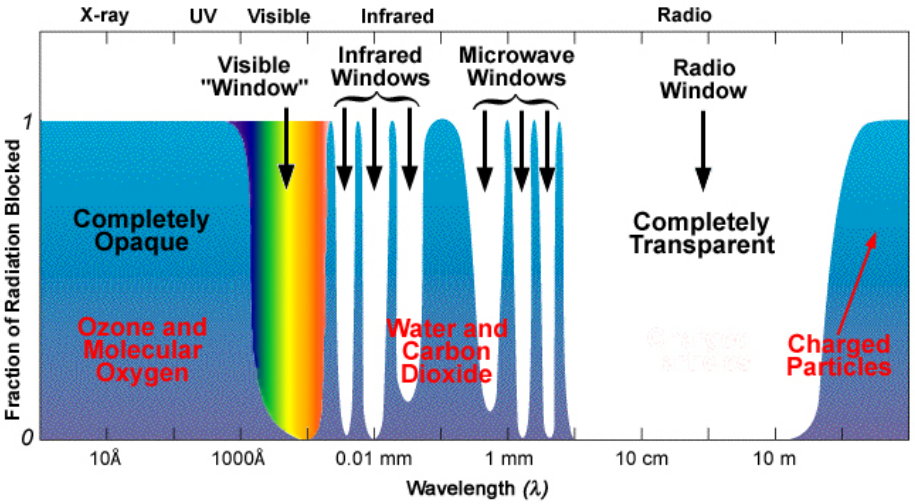

Figure 2.5: Fraction of blocked radiation with respect to the electromagnetic signal wavelength. Note that this figure refers only to the gas-phase composition of the atmosphere.

2.3 Sentinel-1

This thesis exploits open-data acquired by Sentinel-1. This mission is the European Radar Observatory for the Copernicus joint initiative of the European Commission and the European Space Agency(ESA)[Fletcher and ESA, 2012]. Two satellites are currently operating: Sentinel-1A launched in 2014 and Sentinel-1B in 2016. Table 2.1 resumes the main features of the mission. The operational frequency is commonly called C-band and has a 5 cm wavelength. The acquisition mode has 4 different settings. It influences the resolution and the swath size. Interferometric Wide (IW) is the usual setting. However, this system can acquire data in three other methods: Stripmap Mode, Extra Wide Swath Mode, and Wave Mode. The dual-polarization system usually operates with a vertical transmitting signal, so the obtained channels are VV and VH.

The Sentinel-1 mission provides a low revisit time, high geographical coverage, and improved reliability compared to the predecessors. Figure 2.6

Parameter	Value
Operational Frequency	5.405 GHz
Polarization	Dual
Antenna size	12.3m x 0:84m
Height over ground	693 Km
Revisit	6 days
Resolution in azimuth for IW	SLC 20 m
Resolution in range for IW	SLC 5 m
Pixel spacing for IW	GRD 10 m
Swath size for IW	250 Km

Table 2.1: Main features of the Sentinel-1 mission.

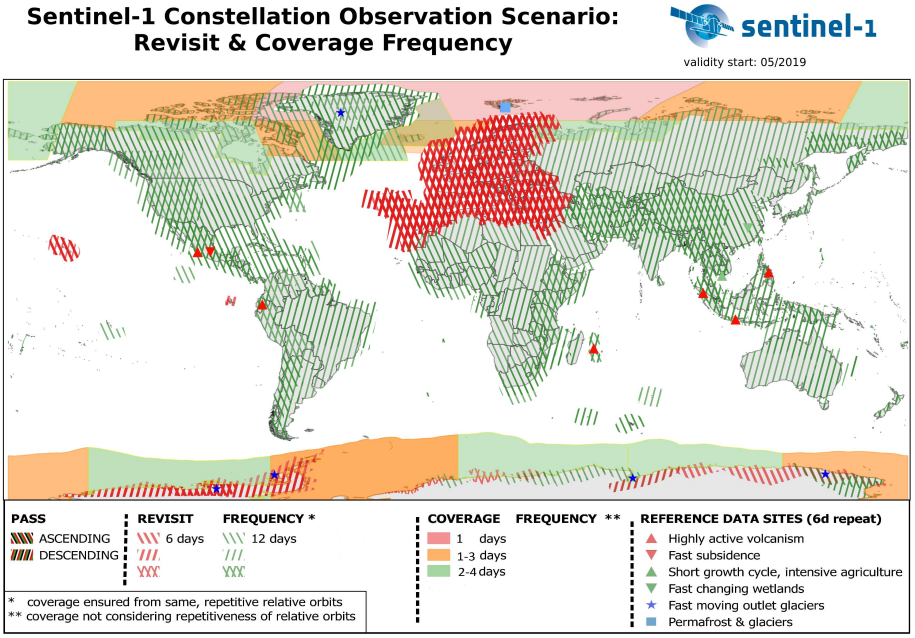

Figure 2.6: The global revisit interval and frequency coverage map of the Sentinel-1 mission.

explains the observation scenario in terms of revisit and coverage frequency for the mission. Revisit frequency indicates the interval between two passes from the same orbit with respect to an earth fixed reference system. On the other end, coverage frequency is the time interval between two acquisitions of the same portion of earth's surface, also if acquired from different orbits. Europe is privileged in the design of acquisitions. The orbits are earth-synchronous. Hence, acquisitions over the same area are at the same

hour. These features make Sentinel-1 a proper mission to perform coastline monitoring.

2.4 Iceye

The current trend in SAR platform design is distinct from traditional approaches in that miniaturized satellites carrying SAR are launched in multiples to form a SAR constellation [Paek et al., 2020]. This can lead to a reduction of costs and to an improvement of temporal resolution. Iceye is a Norwegian company that, exploiting this trend, builds and operates its commercial satellites. The constellation aims at delivering high-resolution data with a high revisit rate. A large number of units is needed to fulfill this mission. By the beginning of 2021, the company has 10 satellites in orbit. They forecast to launch 8 more satellites by the end of 2022. Table 2.2 resumes the main features of the Iceye mission. Note that the reduced satellite size implies a reduction in swath size.

Parameter	Value
Operational Frequency	8 – 12 GHz
Polarization	Single VV
Height over ground	560-580 Km
Revisit	20 hours
Resolution in azimuth for SM	SLC 3 m
Resolution in range for SM	SLC 0.5-2.5 m
Pixel spacing for SM	GRD 10 m
Swath size for SM	30 Km

Table 2.2: Main features of the Iceye mission. SM stands for stripmap mode.

At the beginning of this thesis work, we explored the possibility to use Iceye data. The improved resolution with respect to Sentinel-1 makes this mission suited for precise detection of coastline. The acquisition frequency would also make this mission suited for short-term monitoring. However, the single polarization VV channel could be a problem in the case of high waves. The co-polarized band presents lower contrast between land and sea backscattering than the cross-polarized (VH). Despite the mission's data are proper for coastline detection and monitoring, there were problems with the timing for the request and acceptance of the proposal from the company. Hence, these data were not used, although future developments of this work could include the testing of the proposed algorithms on this data-set.

Chapter 3

Coastline detection and monitoring

In this chapter we start with a state of the art analysis of SAR-based coastline detection and monitoring algorithms. We limit our research to techniques such as statistical machine learning or remote sensing classic algorithms.

In the last years, many neural network (NN) approaches have been proposed but their adoption in a MSc thesis is limited by time-constraints and the need of intensive computational power. In this section we present a novel coastline detection algorithm. It is based on superpixels and aims at filtering the image while preserving the coastline edges.

Finally, we present a monitoring technique based on the visualization of land-cover change dates.

3.1 State of the art

The first steps of the thesis work consisted in exploring the literature. We looked at typical examples of automated coastline extraction from SAR images. The development of algorithms ranges from basic edge detection to more advanced techniques like polarization-based approaches. In the literature, the problem of coastline detection is tackled more than that of coastline change monitoring.

3.1.1 Coastline detection

Speckle is a disturbance for the recognition of the water-land boundary. Many approaches involve filtering as a pre-processing step that degrades the

spatial resolution to improve radiometric resolution [Spinosa et al., 2018]. Adaptive filters for speckle reduction are also applied, and despite being spatially adaptive, they often result in an undesired degradation of the geometric details within the scene under investigation [Oliver and Quegan, 1998]. Improvements are obtained with non-local filters for despeckling, compared to the classic filters like Lee or box-car filter [Urciuoli et al., 2019].

The problem of coastline extraction from SAR imagery can be tackled using two main methods that can be applied independently or in combination: clustering of water and land pixels or edge detection of the interface between land and water. As it was explained in Chapter 2, it is possible to state that backscattering in a water body is generally lower than on land. However, backscattering in the sea increases with the height of waves [Bruno et al., 2019], making the differentiation with land more difficult.

The simplest clustering technique is thresholding. However, it requires the data to be in a single band. The threshold could be defined in many different ways. In the method introduced by [Spinosa et al., 2018], after having despeckled the C-band Sentinel-1 SAR imagery with a 5x5 median kernel, Otsu's method is used to estimate the optimal threshold. This filtering enables the selection of a partition value that minimizes intra-class variance or, equivalently, maximizes inter-class variance [Otsu, 1979]. The binarized result is updated with morphological operations and the borders are selected with a Canny filter.

Another study exploits C-band Radarsat-2 polarimetric SAR data and the thresholding technique [Urciuoli et al., 2019]. The threshold is defined with a constant false alarm rate (CFAR). This method consists of estimating the Rayleigh distribution's parameters after the manual selection of an area that is known to be water. Then, a false alarm rate is chosen and the threshold is extracted from the distribution. As in the previous paper, morphological operations are used to remove tiny features. Finally, a Sobel filter is applied.

Other approaches adopt CFAR, using a different metric than simple backscattering. The product between co- and cross-polarized amplitude channels can be modeled as a Burr distribution. This metric is shown to maximize the contrast between land and water pixels compared to single-polarization in Sentinel-1 SAR data [Ferrentino et al., 2020].

A more complex approach is presented in [Baselice and Ferraioli, 2013], exploiting 3 Cosmo-SkyMed Stripmap images ($3 \cdot 3$ m^2 resolution) acquisitions

and no pre-processing steps. The complex data are co-registered, then local hyper-parameters of a Gaussian Markovian framework are estimated with an expectation-maximization algorithm. In parallel, a low-resolution coherence map of the image is produced to estimate the proportion of water pixels (assuming that non-coherent areas are a water-body). This proportion estimation allows a threshold definition. The final result in the Bagnoli (Campania, Italy) test site is that for 90% of edge pixels, the detection error is two or fewer pixels.

Among the edge detection methods, the most popular approach is to use active contour methods (ACM). These methods, also called snakes, are deformable splines that fit the image edges by minimizing a special energy function. However, ACM can detect only local edges on an image, then some prior information on the contour shape is needed. The method proposed by [Wei et al., 2021] exploits RADARSAT-2 data. The initial shoreline can be obtained with disks disposed in a regular grid over the image. Then, a novel symbolic pressure function modifies the stopping criterion for the classical ACM method. The experiments show improvement compared to ordinary edge detectors.

Finally, an integrated approach with optical data is presented. Optical pansharpened imagery from RASAT is utilized as an initial random forest classification [Demir et al., 2017]. This result is used as training data to define fuzzy parameters for shoreline extraction from SENTINEL-1 data. The accuracy assessment is performed by calculating perpendicular distances between a manually-digitized shoreline and extracted shoreline by the proposed method. As a result, the mean difference is around 1 pixel.

3.1.2 Coastline monitoring

Monitoring a coastline is not a trivial repetition of the coastline detection exercise at different epochs. For example, one of the possible problems that could arise, is that the differences in the detected coastline are actually tidal effects instead of being morphology changes. For this and many other reasons, satellite-based SAR is a better option than optical RS because of its repeatability and consistency, not affected by night and weather conditions.

An analysis of a 5 years time series of ALOS/PALSAR data with HH and HV polarization is presented in [Tanaka et al., 2012]. After median filtering for despeckling the image, the iterative self-organizing data analysis tech-

nique algorithm (ISODATA) was applied. This is an unsupervised form of classification into spectral clusters. The analysis led to identifying that the accretion of two mouth bars at the Mekong River Delta is mainly due to the sediment transportation of sediments by the river. Residuals in the estimated linear model can be correlated with tidal height.

A comprehensive study on the monitoring of the Japanese coasts is carried out in [Tajima et al., 2019]. First, PALSAR-2 images are investigated. The introduced P index defines the probability that the backscattering from a sand beach is higher than the same from the sea. This parameter is used to select suitable images. It depends mainly on the angle-of-sight of the coast with respect to the platform motion and the size of the sand grains. Later, the coastline position is found with a wavelet-transformation. Then the applied method was tested over the time series, leading to a model that correlates the coastline to the water-level.

The approach for coastline detection developed in this thesis exploits a simple thresholding method, but after having segmented with the SLIC algorithm the imagery. On the other hand, the proposed monitoring technique exploits a vast amount of SAR acquisitions from the same orbit, in contrast with the limited use of acquisitions of the described state-of-the-art approaches.

3.2 Coastline detection: a superpixel-based approach

This Section deals with the explanation of the algorithm developed for the detection of the coastline. The method has been validated with Sentinel-1 data obtained through the Google Earth Engine (GEE) platform. However, this approach could be applied with other kinds of SAR amplitude data-sets (acquired with different platforms). Improvement in the results could be achieved using data with a higher spatial resolution. As will be discussed in the result section and according to the state of the art examination, getting a result that is better than half of the spatial resolution is out of reach.

The main idea of the developed algorithm is treating a uniform group of pixels in the image called superpixels. A superpixel can be defined as a group of pixels that share common characteristics. It carries more information than a single pixel and the convenient and compact representation of images can be very useful for subsequent computationally demanding problems. Different algorithms for superpixel segmentation are available, and some were tested (like Quickshift and Felzenszwalb), but the best suited for SAR single-channel scenes is SLIC.

In the next subsections, the single algorithms that compound the process are explained with their advantages and disadvantages. In these subsections, the single steps will be explained in detail. Finally, the coastline-detection method will be described by explaining the subsequent use of the algorithms that compound the process in the Subsection 3.2.4.

3.2.1 SLIC superpixels

Simple linear iterative clustering (SLIC) is a simple and efficient superpixel segmentation method. This method is proven to be faster and to yield a better result than other state-of-the-art methods such as graph-based algorithms like Fezenszwalb and gradient-ascent-based processes like Quick-shift [Achanta et al., 2010]. SLIC is a clustering technique able to segment an image in superpixels, adapting the K-means algorithm in a space that combines color values and image coordinates. In the case of an RGB image, the working space is 5D, while in the case of single-channel SAR data it is 3D. The modification to the classic k-means algorithm consists of reducing the search space of possible pixels for the single superpixel to a delimited neighborhood, usually two times wider than the average shape of the superpixel. This reduction makes the algorithm O(N) complex, hence the computational load is linearly related to the number of pixels in the image. It is worth noting that the complexity is not related to the number of superpixels.

The main parameters that are used for the SLIC algorithm are:

- Number of segments: this parameter defines the number of cluster seeds at the first step of the algorithm. However, the number of segments will vary in the next steps since some superpixels can be merged or split according to their size: a superpixel is split if larger than the maximum size or merged with an adjacent if smaller than the minimum size. The number of segments is inversely related to the size of the superpixel. In this document we will refer to superpixel size, which is independent to the size of the analyzed area;

- Compactness: this parameter defines the relative weight between coordinate features and color features for the space definition. Large compactness yields to a square-shaped superpixel because the coordinate features will be more important than the color features in the distance computation between pixels. On the other end, a smaller compactness leads to a superpixel that fits more the image edges, as the color feature of the pixel is more important.

- Sigma: this parameter is related to the pre-processing step. In fact, the image is smoothed with a Gaussian kernel. This is needed to create a local similarity and the parameter represents the standard deviation in pixels of the smoothing Gaussian kernel. However, in many cases this value is set to tiny values, this yields to minor modifications in the pre-processing phase.

In Figure 3.1 it is possible to appreciate the segmentation obtained with a different number of superpixels and compactness. The data is a stack of 5 Sentinel-1 scenes acquired with the platform on the same orbit over the Lizard Island, Australia. To have an initial despeckling, the median of each pixel is taken. So, the input image to the algorithm is a single channel image with, for every pixel the median value of the pixel intensity in the different acquisitions that compound the stack. Here the VH polarization is used because of its lower backscattering with wave's foam. This region is adopted for the validation of this approach. When the superpixel has a large size, the edge doesn't follow small features, like the small island in the lower right part of the image. For the compactness variation, it is possible to note the squared shape of the edges on the left part of the image while on the right it is possible to note that superpixels follow also objects with smaller contrast than the coastline.

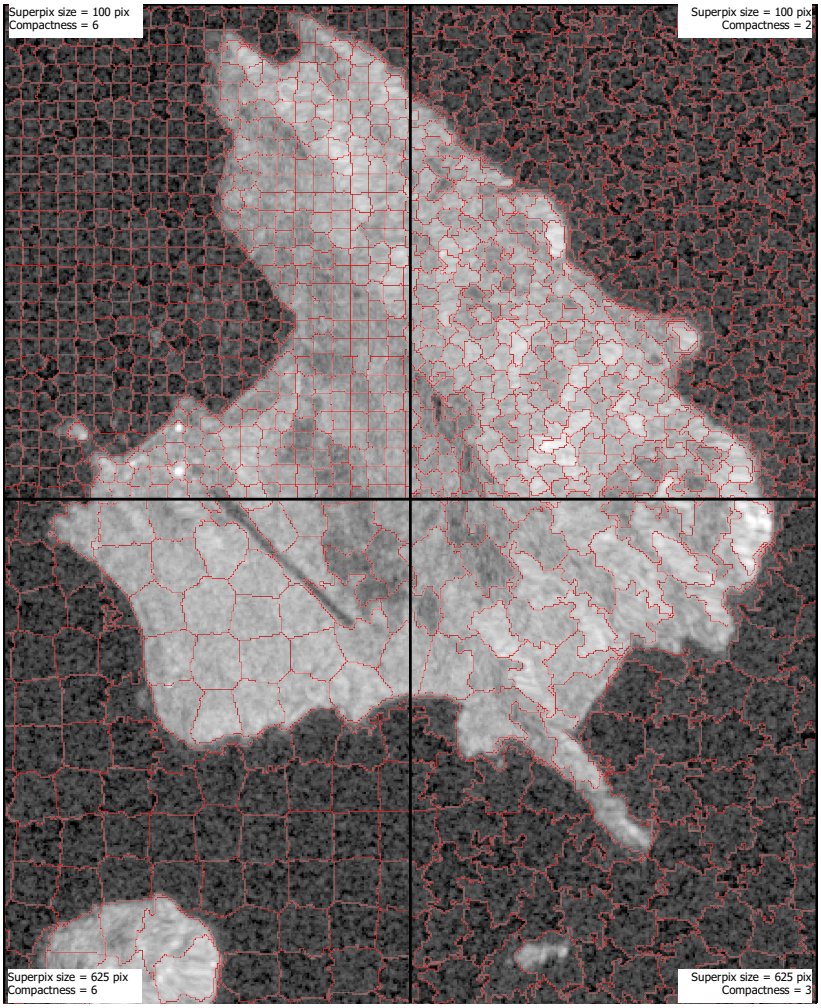

Figure 3.1: SLIC results comparison with different parameters. The original data is a mediated stack of 5 Sentinel-1 VH band acquired over the Lizard island, Australia.

3.2.2 Filtering with superpixels

The superpixels are used as a processing unit for filtering. It is a special case of spatial adaptive filtering with a very flexible filter shape that fits to the morphology of the area. The goal is to erase the speckle effect and at the same time to keep the spatial details that characterize a coastline. The median value of each superpixel is assigned to all the pixels in the group. The median operator is chosen for its robustness against outliers in contrast with the average operator. The main assumption is that the region contained in the same superpixel is uniform. This is not true when objects are smaller than the superpixel size, the result is that those objects are erased by the

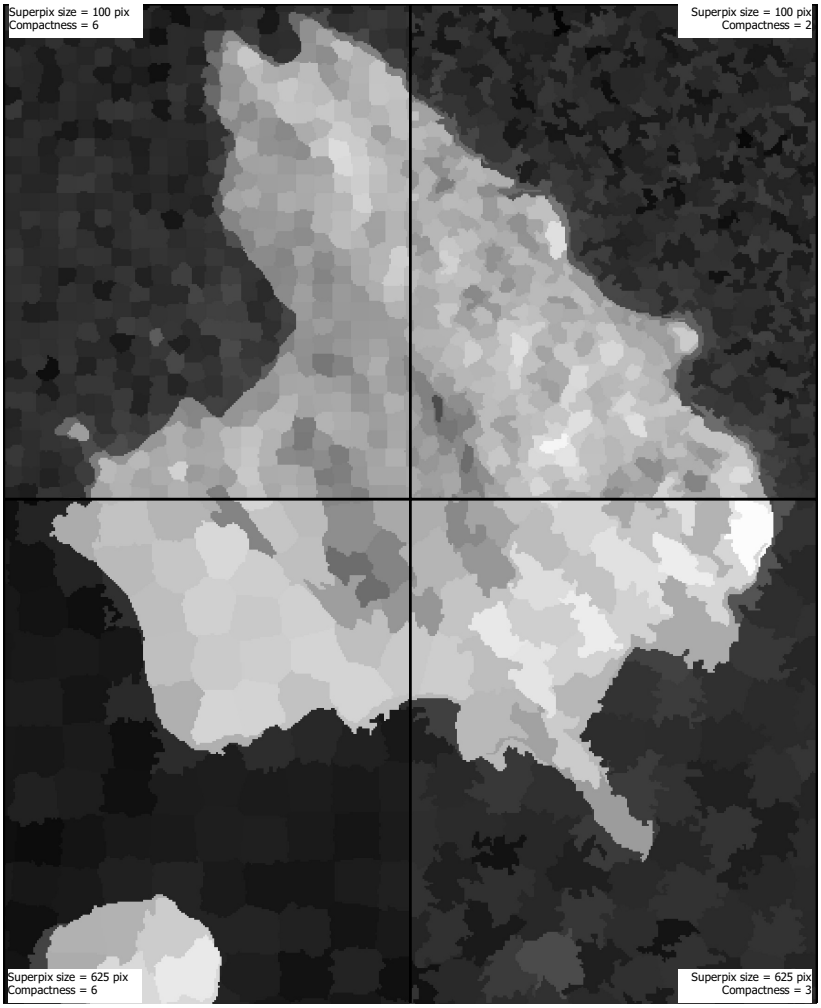

Figure 3.2: Median filtering based on the superpixels region. The original data is a stack of 5 Sentinel-1 VH band acquired over the Lizard island, Australia.

filtering. However, since the goal is to detect the main coastline, this is not a problem. As explained in the state of the art, every spatial filtering operation induces a loss in spatial resolution. The ratio in our work is that the superpixel can follow with fidelity the coastline, hence the filtering does not degrade the definition of the detected coastline.

In Figure 3.2 the filtering effect with different superpixel size is shown. As it happens with other kinds of filters, the larger the size, the greater the filtering effect. The lower part of the image has 625 pixels per superpixel, while in upper part has just 100 pixels. A minor variability is present in the lower part as effect of an higher smoothing. The left part of the figure exhibits a minor variability with respect to the corresponding right part.

It happens because flexible superpixels can follow image features. Hence, not-compact superpixels are more homogeneous than compact ones, and the filtering effect is slightly lower.

3.2.3 Thresholding

After the SAR scenery is segmented in superpixels and properly filtered, the subsequent step is to identify land and water superpixels. As explained in the pixel brightness subsection, water pixels present a characteristic low backscattering. This property is due to water smoothness. On the other hand, the land surface presents a high backscattering because of its larger roughness. As it is clear from Figure 3.3, the histogram (blue colored) of a SAR scene filtered with the described methods presents a bimodal distribution.

The task is now to define a suitable threshold that partitions the classes of water and land based on the single channel information of backscattering amplitude. Two different methods are selected for the definition of the partition value. The methods differ in the sense that their objective is different. However, results are very similar in many of the tested areas. The showed dataset refers to the Lizard island region. The size of the scene is about 35 km^2. When applying these algorithms, there's the need to represent both land and water areas in the histogram, with a proper fraction of the image belonging to each class. Otherwise, the bimodality of the histogram is lost and also the possibility to partition the superpixels.

Otsu's method

Otsu's method is a non-parametric and unsupervised method of automatic threshold selection for picture segmentation [Otsu, 1979]. It can efficiently identify the optimal partition value for a bimodal histogram. The objective function is the inter-class variance, and it is maximized. Note that the goal is the same as intra-class variance minimization. In Figure 3.3 the bi-modal histogram of the Lizard Island is shown with the threshold obtained with the Otsu's method. This result can be seen in Figure 3.5 in square 3 translated in the map by highlighting the boundaries of the defined classes.

Gaussian Mixture

A mixture model is a probabilistic model for representing the presence of subpopulations within an overall population. For the problem of a SAR scene of a coastal region, the prior hypothesis is the presence of two groups of pixels,

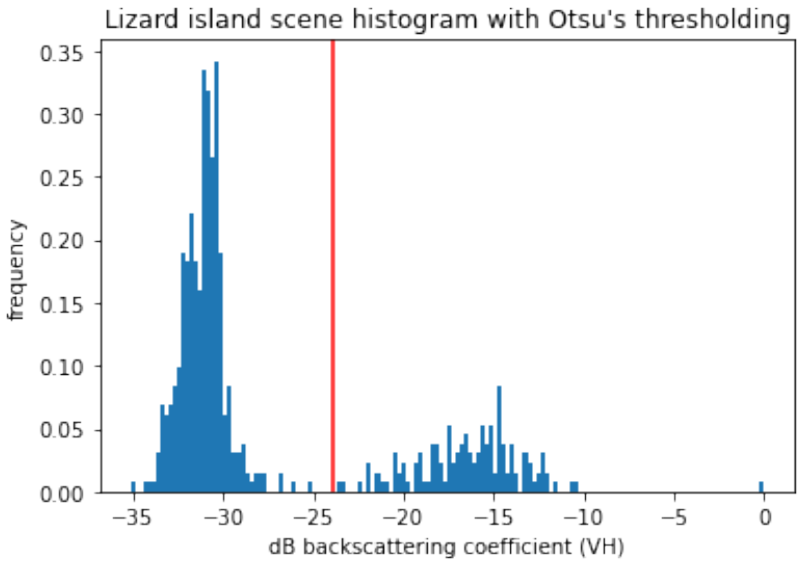

Figure 3.3: The histogram for the Lizard island scene depicted in Figure 3.1. The result of the Otsu's method (in red) is equal to -23.95 dB

representing the sea and land pixels. In the section related to the speckle description, we discussed that in a homogeneous area with distributed targets the backscattering could be modeled with a Rayleigh distribution. However, in this problem the sub-populations are not homogeneous: land pixels contain different covering like sand, bare ground, different vegetation types, urban areas. For this reason, we assume the sub-populations to be well modeled by a Gaussian distribution. The problem is to estimate the parameters (μ and σ) of the two Gaussian Distribution functions. In addition, also the proportion of the land and water superpixels needs to be estimated in order to depict the entire superpixel distribution of the scene. The population with a lower mean represents water pixels, while the other represents land pixels.

The intersection between the two distributions is the optimal value for separation. It will yield the minimum theoretical error in classification. It is possible to check the result of this algorithm for Lizard island data in Figure 3.4. One of the positives of this algorithm is that it is possible to estimate the theoretical error rate. The area below the orange curve and on the right of the threshold represents the false sea superpixels rate. Respectively, the area below the black curve and on the left of the threshold is the false land superpixel rate.

As you can see from the comparison between the two graphs, there are two superpixels assigned differently in the two cases. The test is carried

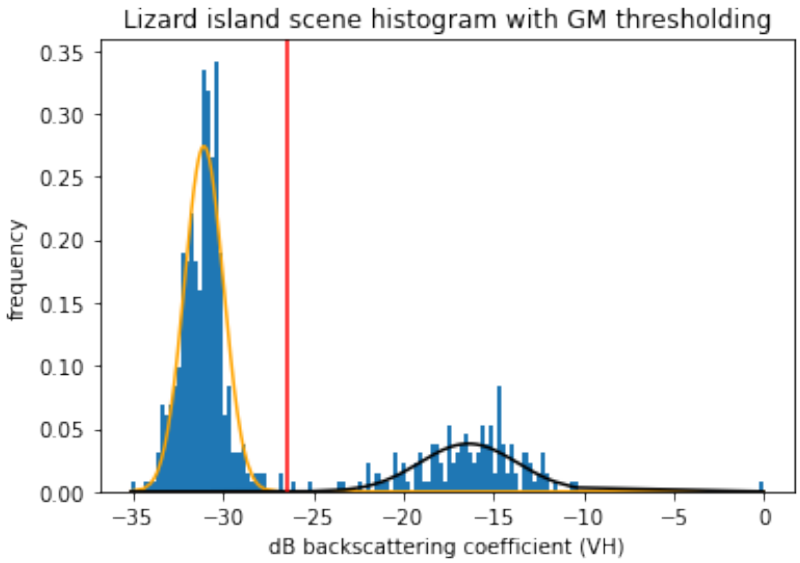

Figure 3.4: The histogram (blue) with the estimated gaussian PDFs (orange and black) for the Lizard island scene depicted in Figure 3.1. The threshold (in red) results equal to -26.48 dB.

out in many regions, with different SLIC parameters, and with different land-sea proportions. There's not a trend with one thresholding technique systematically over-performing the other. The errors of both techniques tend to be uniformly divided between false land superpixels and false water superpixels. For this reason, in this work both the techniques are considered proper for the task of thresholding.

3.2.4 Iterative routine

When segmenting an image with the SLIC algorithm, a trade-off is present. The larger the superpixel the larger the filtering effect, hence small features (like tiny islands and small water bodies inside the coast) can be disregarded. On the other end, the larger the superpixel the worst the edge will follow the coastline details. This fact led to the idea of an iterative method. For the following example, the original image is generated by a 5 images stack with the Sentinel-1 VH-polarized band. Note that for different areas with different features or scenes with different size, the algorithm could be modified in its parameters or even in the number of iterations. The steps for the coastline detection algorithm are described here and pictured in Figure 3.5. The first four steps perform a rough coastline detection, while the remaining will refine the result.

1. Large superpixel segmentation: the parameters for the first segmentation with the SLIC algorithm are:
    - Superpixel size: 400 pixels
    - Compactness: 3
    - Sigma: 1
2. Median filtering: the superpixels are filtered by assigning to the whole superpixel the median value of its pixels.
3. Thresholding: in this case the method chosen is Otsu's method. In panel 3, the borders between the land and water clusters are shown.
4. Coast selection: the superpixels that lie at a maximum distance of 50 m from the borders highlighted in panel 3 are selected.
5. Small superpixel segmentation: the selected part of the original image is segmented again with the SLIC algorithm. The superpixel size is decreased to be able to follow the coastline with greater accuracy. The parameters are:
    - Superpixel size: 60 pixels
    - Compactness: 1.5
    - Sigma: 1
6. The filtering is performed again with the median operator: the median value of each superpixel is assigned to the pixels in the group. In this step, the selected areas are finely filtered. However, in panel 6 also larger superpixels are shown in the not-selected region. It is possible to see how the smaller superpixel has a smaller filtering power.
7. The final result is shown against the original data and the result is satisfactory at the first look. Further analysis of the results are carried out in the next chapter.

In the next chapter, the results of this algorithm will be compared to an optical imagery relative to the same period.

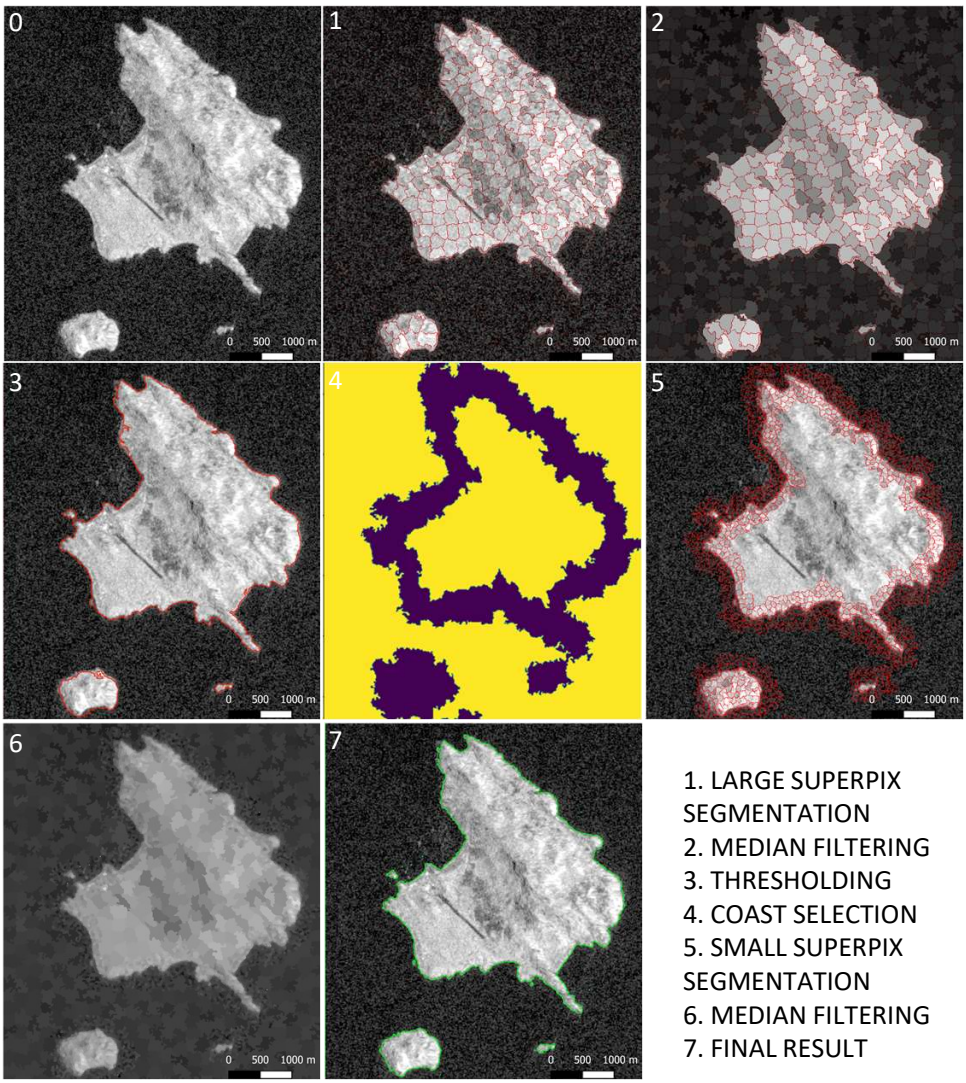

Figure 3.5: Pictorial representation of the algorithm steps. In general the first 4 steps are a rough selection of the coastline are, later the refinement is carried out. The thresholding technique is for both cases Otsu's method.

3.3 Coastline monitoring: a change visualization method

The Sentinel-1 mission, because of its revisit time, is ideal for monitoring. It is crucial to stress that monitoring in the case of a complex phenomenon as the coastline position is not just comparing two positions in time. Tides and

other phenomena like erosion and accretion make this problem more complex. We explain here the monitoring method for Reentrâncias Maranhenses. This area will be delineated in Chapter 4, where the results will be analyzed.

3.3.1 Data selection and preparation

A large portion of the Sentinel-1 dataset for this specific area of about 75 km^2 is exploited. The time series consist of four years of consistent acquisitions, as the full activity of the mission begun in late 2016. In the following we list the preprocessing operations:

1. The acquisitions are grouped by season, for a total of 16 seasons. The season with the least number of scenes has 7 measurements, hence this number of acquisitions is selected for each season.

2. For every acquisition the product of the cross- and co-polarized channels is computed and adopted as metric:

$$r = \sigma_{\mathrm{vv}} \cdot \sigma_{\mathrm{vh}}$$

3. A pixel-wise temporal filter on the 7 images stack is applied through the average operator.

The r metric is chosen because it maximizes the land-sea contrast. Moreover, working with a single band that combines information of different nature is an advantage in terms of simplicity. An equal number of acquisitions for each season should be considered. When the average operator is applied, the reduction in the speckle presence is proportional to the number of considered scenes. Each product should have the same reduction rate. The averaging with 7 acquisitions and over a period of three months has the following benefits:

- speckle reduction;
- erase of temporary effects due to extreme events;
- tidal variation removal.

3.3.2 Backscattering and sea state

The monitoring task requires the comparison between different sea states in time. SAR systems provide a great opportunity because of the orbit repetition and constant illumination. The backscattering from the land areas

also presents stability when no changes occur. However, sea backscattering is not constant in time: it varies with the sea roughness. Waves can substantially modify the sea surface, leading to some specular reflection in the platform's direction. Waves are related to meteorological events, like wind and rain. Figure 3.6 [Tajima et al., 2019] shows the relation between backscattering intensity in water and wave height. The mission is PALSAR-2 L-band. $\sigma_{\mathrm{s}} - \sigma_{\mathrm{s0}}$ should represent the backscattering coefficient of the sea, excluding the influence of the angle between the beach direction and the platform path. A clear positive correlation is shown. The C-band suffers, as well as L-band, from an increase in RCS when the wind speed (hence also wave height) increases [Mouche et al., 2006].

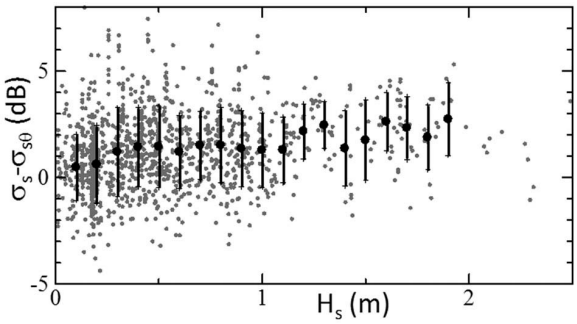

Figure 3.6: Relation between amplitude and significant wave height, Hs. Gray dots are the data obtained from each scene, black solid circles are the average of obtained data and vertical bar indicates the range of the standard deviation of the obtained data. From [Tajima et al., 2019].

3.3.3 Introduction of *NLWI*

Despite the averaging of 7 acquisitions for the development of a scene that represents the state of the coast in a whole season, the r metric still shows variations in time in the sea area. Figure 3.7 depicts this by showing different histograms. Each histogram represents a season, all are bi-modal with the left side representing the sea portion of the image (low r value) while the right-side is the land portion of the image. While the land part of the histogram presents a certain homogeneity, sea pixels present a great intensity variation. The normalized land-water index is proposed to compare SAR scenery acquired with the sea in different states. This index exploits the single-channel information of the r metric.

$$NLWI_{i,j} = \frac{r_{i,j} - T_i}{\mu_i^l - \mu_i^s}$$

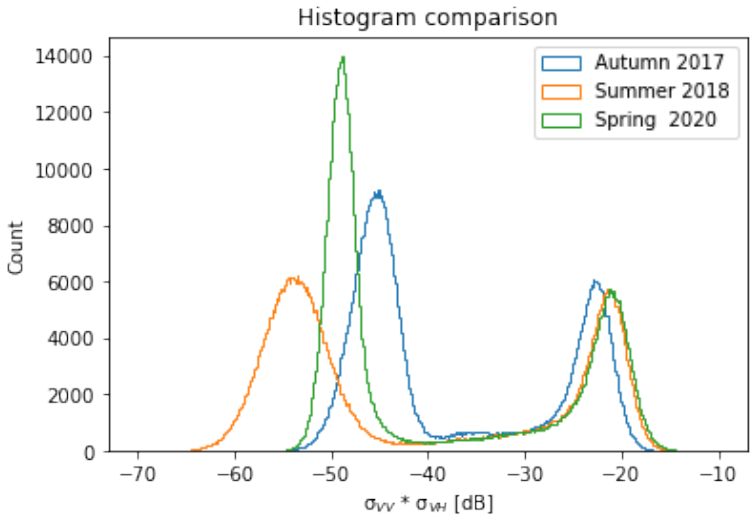

Figure 3.7: Comparison of histograms for three scenes. Each scene represent a 3 month period and is the pixel-wise average of 7 r metric scenes.

In the formula, the i is the season scene index while j is the pixel index. Each image is stretched and shifted depending on the seasonal scene parameters. In each seasonal scene i the Gaussian mixture parameters are estimated. The symbols μ_i^l and μ_i^s are respectively the means of the estimated Gaussian distribution for the land and sea sub-populations of the histogram. Moreover, the threshold T_i is estimated as the intersection point of the two distributions. Figure 3.8 shows the results of the estimation for the parameters involved in the *NLWI* computation. This computation is done for every studied season, Table 3.1 shows the results. It is worth noting the differences between the seasons, with a gap of nearly 7 dB between the largest and smallest threshold.

The goal of adopting *NLWI* is to enable comparison between scenes representing different seasons. This index has a particular histogram with positive values assigned to pixels resembling land backscattering and negative values assigned to pixels resembling sea backscattering. As Figure 3.9 shows, the land and water clusters are centered respectively in +1, -1. It is worth noting the decrease in the difference of histograms between this and Figure 3.7.

3.3.4 Modeling of *NLWI*

Through *NLWI*, inter-temporal comparison of pixel values is possible. The effect of different sea states is erased. Many pixels will present a variation, but the monitoring task requires the detection of areas that change the cov-

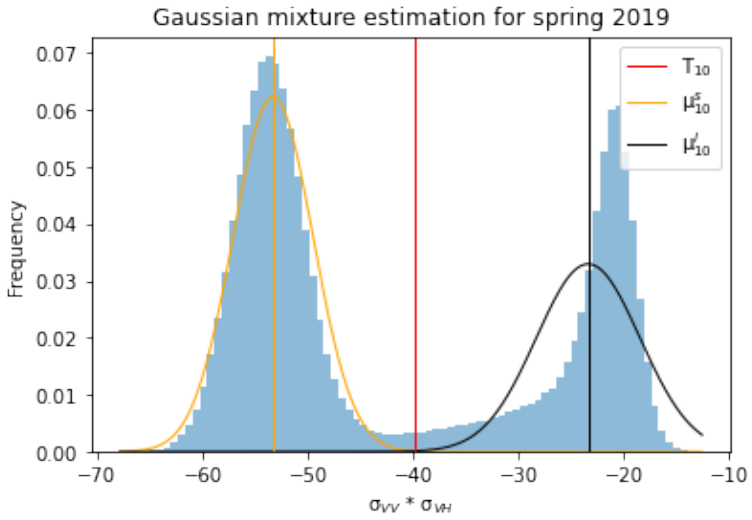

Figure 3.8: Gaussian mixture estimation for the parameters involved in the NLWI metric for the Spring 2019 scene. $\mu_{10}^{l} = -23.3\,dB;\ T_{10} = -39.9\,dB;\ \mu_{10}^{s} = -53.3\,dB$

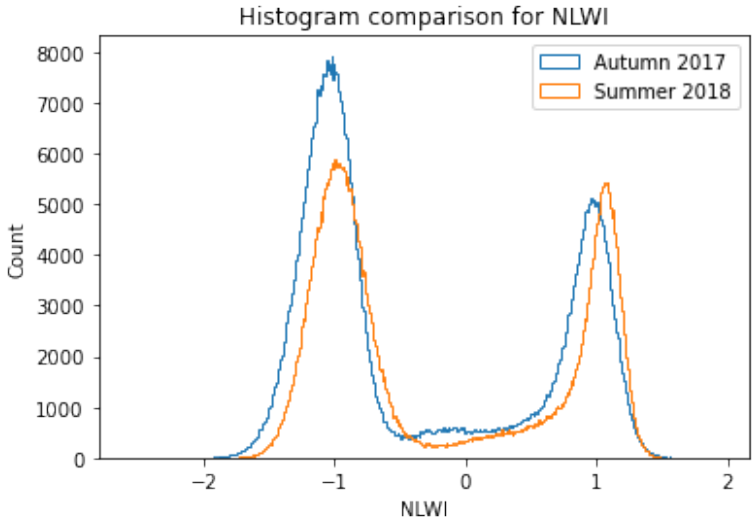

Figure 3.9: Histogram for NLWI index.

ering. Both eroded and accretion areas should be identified. Besides, also the date when the change happened, is an important parameter that could be estimated. Many models are appropriate for a pixel-wise analysis, and the adoption of one depends mainly on the dynamic present in the study area. The model we adopted is a simple linear model. Two parameters, angular coefficient and intercept, are estimated pixel-wise. This solution enables the

season	μ_i^s	T_i	μ_i^l
winter 2017	-49.9	-38.9	-24.3
spring 2017	-49.7	-39.3	-24.4
summer 2017	-45.4	-36.5	-24.6
autumn 2017	-46.3	-36.8	-25.2
winter 2018	-50.2	-38.0	-24.2
spring 2018	-53.5	-40.1	-23.9
summer 2018	-49.4	-36.9	-24.6
autumn 2018	-51.3	-38.0	-25.3
winter 2019	-53.8	-38.8	-23.7
spring 2019	-53.3	-39.9	-23.4
summer 2019	-50.8	-39.0	-25.0
autumn 2019	-50.9	-38.1	-25.6
winter 2020	-49.5	-42.2	-24.7
spring 2020	-48.9	-42.3	-24.0
summer 2020	-46.9	-40.8	-25.4
autumn 2020	-46.3	-39.7	-26.1

Table 3.1: Parameters estimated for each season necessary to the estimation of NLWI

detection of the pixels with a land-use change. Figure 3.10 shows the model fitting to data belonging to areas with different behavior. The two upper squares represent pixels that are stable in their land-covering. They are characterized by a very low angular coefficient and no intersection with the land-sea border. The lower squares represent pixels that change the land-use in the analysis time-span. The left one depicts an area with beach accretion. The right one depicts an erosion phenomenon: at the beginning, the pixel was classified as land while from spring 2017 on the pixel is classified as sea. In this pixel, note the capability of the model to estimate a change-date close to the boundary of the time series. The angular coefficient of the estimated model can be considered as the velocity of accretion or erosion of a certain area. However, this can be stated just for pixels that present an horizontal intercept in the analyzed period.

In the next subsection visualization methods to depict the coastal modifications over the 2017-2020 period will be explained.

3.3.5 A visualization of change date

The model and the other methods presented in this section can extract information from the large SAR data-set. However, an appropriate visualization

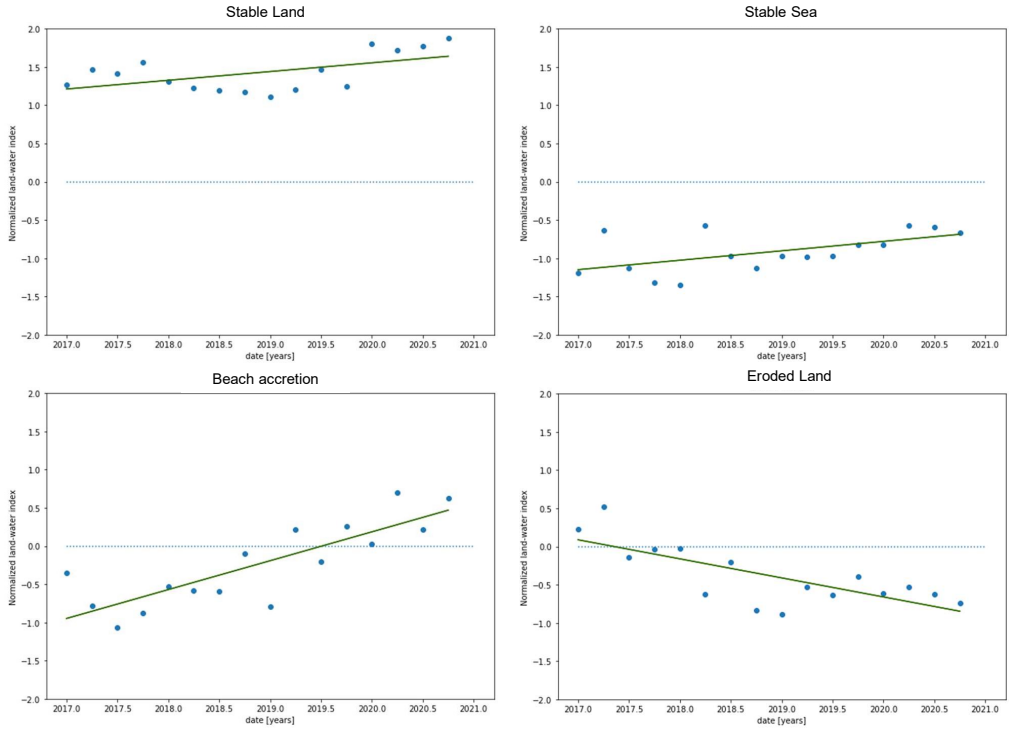

Figure 3.10: Linear regression for single pixels belonging to different groups. Each point in the time series is the NLWI resuming the pixel state for a whole season. In the two squares above represent stable areas. The lower squares represent two dynamic pixels that mutates the land-cover.

of the change date is necessary to allow a proper interpretation. As usual, when dealing with geographical data a map is the best option. The focus here is on the visualization of the change date. The classic RGB color model is more common in computer graphics. It relies on the same principle as human vision, but it cannot describe single information over the color spectrum.

In contrast, we adopted the hue, saturation, value (HSV) color model. It was developed to align with human perceive color-making attributes. Figure 3.11 depicts the HSV color space as a cylinder. The Hue represents the color angle on the cylinder. A 0° hue results in red, 120° results in green, and 240° results in blue. This attribute carries the most important information. Saturation controls the amount of color used. A color with 100% saturation will be the purest color possible (depending on the hue), while 0% saturation yields a greyscale (depending on the value). Value controls the brightness of the color. A color with 0% brightness is pure black while a color with 100% brightness has no black mixed into the color.

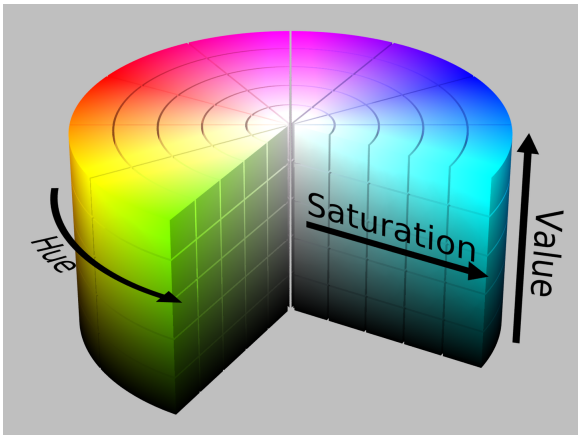

Figure 3.11: HSV representation of color space

Adopting HSV color codification allows to optimally display the change in the coastal position. We propose the visualization of gained or lost land by displaying only pixels that present a horizontal intercept in the time boundaries of the analysis. In this way we can exclude areas that do not present any change in the class over time. Each highlighted pixel exhibits the following attributes:

- Horizontal intercept of the *NLWI* vs time model (date of the change in land covering) as hue. The hue cylinder is sliced in the last 30% to avoid similar colors in the two boundaries. Hence, the cylinder is sliced to nearly 270°, ranging from red to blue.

- Post-change average *NLWI* as value. The closer the *NLWI* to the new cover (± 1) the higher the value. In this way, the change-date interpretation is clear for pixels with high value, while areas with an *NLWI* post-change close to 0 will be shown in black.

- Mean squared error (MSE) for the model as saturation: the smaller the MSE the larger the saturation. In this way, the change-date interpretation is clear for pixels that show a low MSE. On the other end, if a pixel doesn't follow the model at all will appear white.

Figure 3.12 depicts the erosion of an area in the study area of the Reentrâncias Maranhenses. The colored pixels are coded according to the rules previously explained. Hence, each colored pixel was land at the beginning of the analyzed interval and is a sea pixel at the end. The hue is defined according to the modeled time of change in cover. In the background, there is grey-scale SAR data that represent the last season of the analysis. It is possible to

appreciate the slow and steady erosion of the coastal area. An analysis of the results will be carried out in the next chapter.

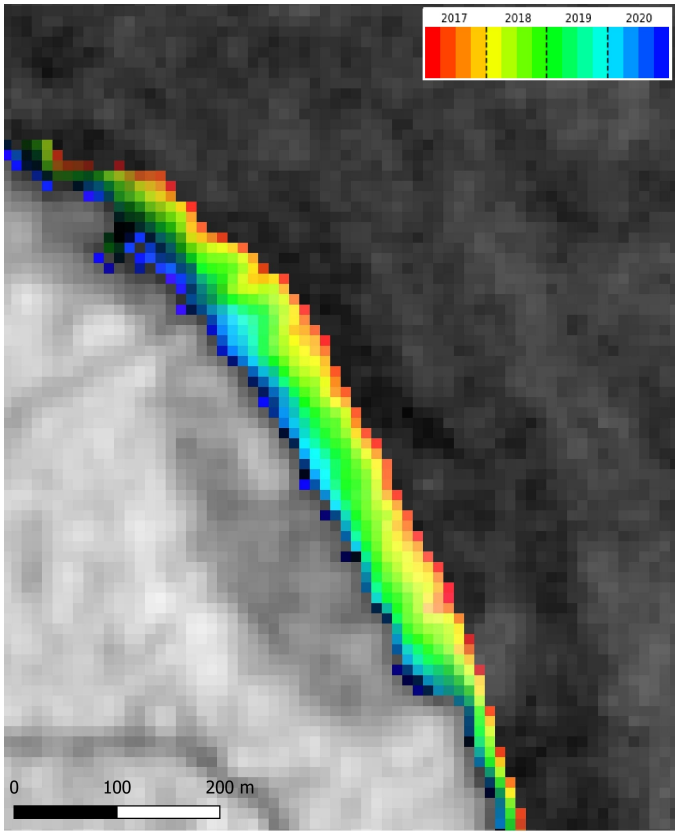

Figure 3.12: Depiction of an eroded coastline in the natural area of the Reentrâncias Maranhenses. The visualization of the loss-date estimated by the NLWI model allows a quick understanding of the dynamic. The background is SAR data that represent the last season (autumn 2020) of the analysis.

Chapter 4

Case studies

This chapter deals with the explanation of case studies and the analysis of the results. In the first section, a brief description of Google Earth Engine (GEE) and the delineation of its capabilities for exploratory data analysis in the context of this thesis is done. Secondly, we discuss the validation for the coastline detection method carried out over the Lizard Island site: the detected coastline is compared to a line determined manually with an optical scene as background. An application for the coastline detection algorithm is described in the third section, with the presentation of dataset statistics for the study of tidal plains in the Bay of Fundy area. Finally, the results of the monitoring method in the Reentrâncias Maranhenses area are shown. The validation is carried out by comparison with the optical and with the detected coastline from a deep learning (DL) algorithm.

4.1 GEE for exploratory data analysis

In recent years, due to technological advances, to the launch of several satellites from various government and intergovernmental agencies and to the open-data policy, the amount of earth observation (EO) data freely available has increased quickly. Only in 2019, the volume of open data produced by Landsat-7 and Landsat-8, MODIS (Terra and Aqua units), and the three first Sentinel missions (Sentinel-1, -2, and -3) is around 5 PB [Soille et al., 2018]. It is clear that this amount of data cannot be stored, analyzed and processed on a normal PC. From here comes the need for new technologies for Spatial Data Infrastructures (SDI) to properly work with big EO data sets.

4.1.1 The spread of Spatial Data Infrastructures and cloud computation.

SDIs were historically a data-access technology, but lately, they incorporated the Moving Code paradigm. This new idea consists in providing the user, thanks to cloud computing and distributed system, computational power to execute applications server-side [Muller et al., 2010]. The source code is sent to the servers to be executed, instead of sending the dataset to the user. As previously stated, this happens because of the big nature of EO data, and because new technologies made this possible. This change has been embraced by both the public (for example see the DIAS program, from the ESA) and the private sector (with big EO data public on Amazon web services platform). In this context, [Gomes et al., 2020] defines "Platforms for big EO Data Management and Analysis" as computational solutions that provide functionalities for EO data management, storage, and access; that allow the processing on the server-side without having to download big amounts of EO data sets; and that provide a certain level of data and processing abstractions for EO community users and researchers. In the following subsection, Google Earth Engine (GEE) – the platform adopted for this thesis– is presented.

4.1.2 Google Earth Engine

GEE is a cloud-based platform that enables large-scale analysis and visualization of geospatial data sets. It was launched in 2010 by Google as a proprietary system and it is available to users as a free service for small and medium workloads, using a business model similar to the other cloud-based services of the company [Gorelick et al., 2017]. GEE provides a JavaScript API and a Python API for data management and analysis. For the JavaScript version, a web tool is available. Therefore, the user has easy access to available data, applications, and real-time visualization of the processing results. This platform provides a data catalog including a large repository of geospatial data. The SAR products available on the platform are Sentinel-1 imagery and ALOS/PALSAR composites (like Forest map and yearly composites). Before being made available, these data sets are preprocessed, enabling efficient access and removing many barriers associated with data management. As for Sentinel-1 data, each scene is pre-processed with Sentinel-1 Toolbox using the following steps:

1. Thermal noise removal;

2. Radiometric calibration;

3. Terrain correction using SRTM 30 or ASTER DEM for areas greater than 60 degrees latitude, where SRTM is not available.

4. Conversion of the final terrain-corrected values to decibels via logarithmic scaling.

The user can process and analyze data available in the GEE public catalog with a library of functions. These functions are implemented in a parallel processing system that automatically splits the computation to perform it in a distributed environment. Processing only occurs when there is an output (visualization or writing) to compute. This lazy computation mode allows the processing of only some parts of the data that actually produce the required output. The result of processing can be viewed in the web tool or saved in Google Drive. One facility that GEE provides to users is the capability to share their scripts and assets with other users of the platform. Nevertheless, these scripts use algorithms implemented internally by the platform, and these algorithms are close and can not be extended on the server-side. Therefore, GEE can not guarantee that an analysis performed on the platform can be reproduced in the future since these internal algorithms can be changed or discontinued by the platform at any time. The GEE terms of service guarantee users the intellectual property of their codes and data as well as that the company will not use such information for purposes other than what is necessary to provide the service to the user.

When working with SAR data, it is often hard to compare data without downloading it. During this thesis work, GEE has proven to be a great tool in terms of data visualization, preprocessing and preliminary analysis. GEE allows easy visualization of SAR data-sets before downloading. Allowing the user to download only the necessary region and scenes eases the computational burden for large volumes of data. The execution of many preprocessing steps explained in the previous chapter is server-side. For example, the time-series for monitoring are compound on a season basis and with pixel-wise temporal filtering. In that case, I had to download just 16 season images of a 75 km^2 area. If I had to do this computation on my laptop that would have required downloading 112 images of the whole SAR acquisition. The studied area is not vast in this case, but for wider investigations, the adoption of GEE would make the difference. In the following sections, some examples of the platform used for preliminary analysis are presented.

4.2 Coastline detection: the Lizard Island

The results for the proposed iterative routine are analyzed. The implementation details are explained in Section 3.2.4. The following paragraph is a brief recap. The initial data-set is a stack of 5 Sentinel-1 VH-polarized C-band images. It is acquired and preprocessed through GEE, hence the data was treated as we explained in the previous section. The process that this thesis proposes involves two iterations: the first is supposed to individuate roughly the coastline and to filter out tiny islands that are not on the main coastline region. Superpixels individuated with the SLIC algorithm are partitioned in land and sea groups with Otsu's thresholding method. The border between the two clusters is taken as an approximate coastline. In a second step, the superpixels that lie in the 50 m range from the approximated coastline are selected for a finer segmentation always with SLIC. The final partition is executed again with Otsu's technique. Figure 4.1 compares the detected coastline and Planet SkySat imagery with a 0.8 m pixel spacing. In the figure, there is also a manual digitized coastline using as background the optical dataset.

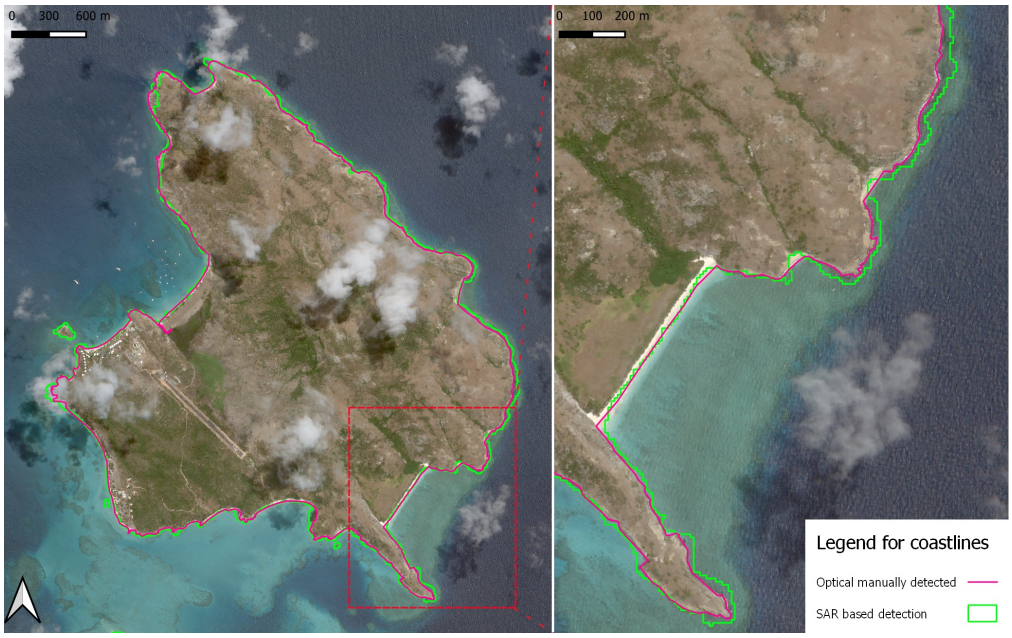

Figure 4.1: The SAR based detected coastline (in green) extracted with the process explained in Section 3.2.4 is compared to the manually digitized coastline (in green) based on the optical imagery Planet SkySat (0.8 m pixel spacing), by ©Planet Labs Inc. On the right there is an enlarged view to appreciate finer details.

In general, it is possible to state that there are no apparent georeferencing

problems, as there is not a systematic direction of the error. In the western part of the island, the detected coastline is - in many sections - so close to the manual detected one that the two lines are overlapped. In the enlarged part, on the right, it seems that the detected coastline follows better the background reference in the sandy beach. On the other end, the detection is worse on high coasts. Where the terrain morphology presents cliffs or high sloppy areas: mechanisms like shadowing or multiple bounces could make the backscattering from those areas resemble the sea.

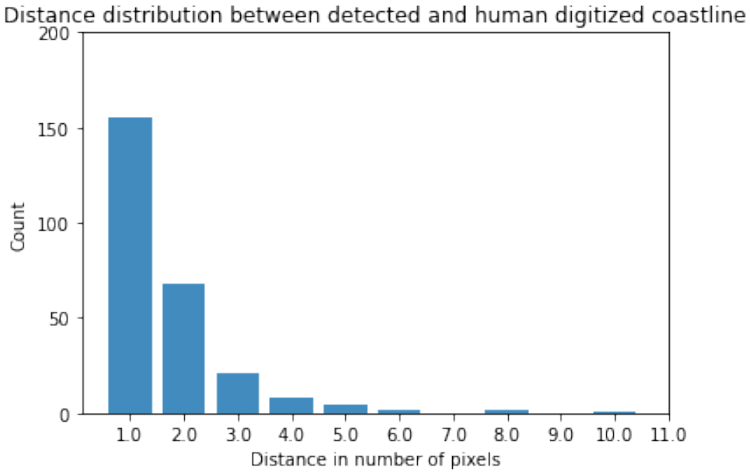

Figure 4.2: The graph depicts the distribution of the distance between 363 points equally spaced by 50 m on the manually digitized coastline visible in Figure 4.1 and their closest point on the coastline detected by the proposed algorithm.

The adherence of the detected coastline to the optical imagery of the shoreline is tested. On the manually digitized coastline, points are selected with a 50 m spacing. For each point, the minimum distance from the detected shoreline is computed. Figure 4.2 depicts the distribution of the computed distances grouped by the pixel sixe of 10 m. Each point for which the distance is lower than ten meters (the pixel spacing) will fall in the first bin. The vast majority of the selected points lie closer than twenty meters from the digitized counterpart. The average distance is 12.63 m. To contextualize this number it is crucial to note that the pixel spacing is ten meters, but the resolution for the GRD product used for the computation varies between $20.4 \cdot 22.5\ m^2$ and $20.5 \cdot 22.6\ m^2$ (range $\cdot$ azimuth) depending on the incident angle. The minimum distance between two objects that a measurement instrument can distinguish is its resolution. The task of getting results in an average distance closer than half of the resolution is hard.

Figure 4.3 depicts the cumulative distribution. It is possible to appreciate

that for 80% of the points, the distance is less or equal to 20 m. For 95% of the points the distance is smaller than 30 m.

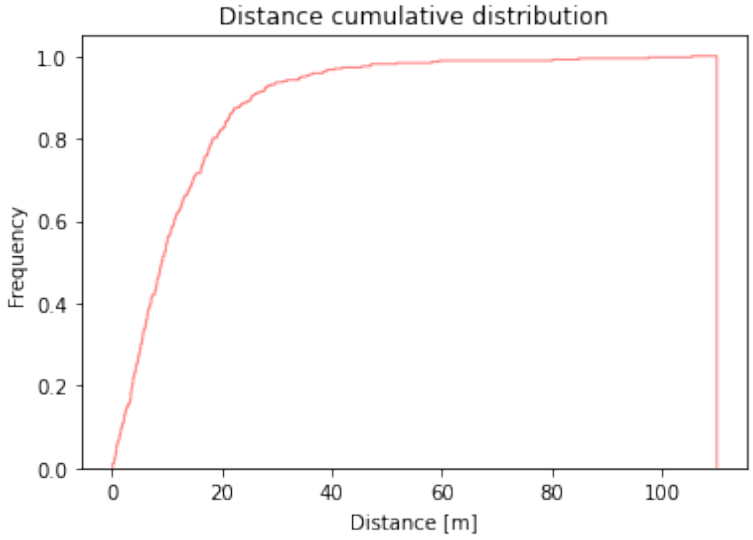

Figure 4.3: The graph depicts the cumulative distribution of the distance between points 363 points equally spaced by 50 m on the manually digitized coastline visible in Figure 4.1 and their closest point on the coastline detected by the proposed algorithm.

4.3 Tidal plain detection: the Bay of Fundy

Figure 4.4: Photographic comparison of the Bay of Fundy high and low tide.

In this Section the case of a coastline that oscillates for the tidal variation is presented. Adopting the same approach of the previous Section would not depict the presence of tidal plains that are large and flat inter-tidal regions. A coastline detection applied on acquisitions with extreme tide events combined with the analysis of the long dataset statistics is necessary.

The Bay of Fundy separates the Canadian provinces of New Brunswick and Nova Scotia. The region is known for the highest tides in the world. The tidal range in the Bay of Fundy can reach 16 m. This phenomenon happens because normal oscillations are amplified by the tidal resonance in the funnel-shaped bay. In Figure 4.4, a photographic comparison between low and high tide events is shown. This analysis will focus on the harbor city of Fundy, which has a large tidal plain well visible with the Sentinel-1 resolution. The exploratory data analysis that led to the selection of this specific area is explained in the following subsection together with the adopted GEE algorithms. The computation is server-side and the repetition for other cases is a quick task. Later, an in-depth analysis adopting the coastline detection method is carried out.

4.3.1 Exploratory data analysis

GEE allows the user to compound images by assembling bands from Sentinel-1 acquisitions in different periods. Two scenes with high and low tide are selected. The first image was acquired on 19/01/2020 at 18:19 (local time). The high tide event that day was at 18:50, with a predicted sea level of 7.48 m. The sea level at the scene acquiring time can be estimated as 7.25 m. The second image was acquired on 26/01/2020 at 18:19 (local time). The low tide event was at 19:08, with a predicted sea level of 0.87 m. The sea level at the scene acquiring time is estimated around 1 m.

The comparison between the two images is carried out by assigning the

scene with the high tide event to red and green channels (the equivalent of a yellow band), while the scene with the low tide event is set as the blue band. The result will highlight the differences between the two acquisitions that differ just for the water level. Thanks to the SAR acquisition scheme, the geometry of acquisition and illumination remain the same. The result is shown in Figure 4.5. The goal of this analysis is to identify the tidal plains that are highlighted in blue. These areas present a high backscattering in the low tide scene and a low backscattering in the high tide scene. Hence, the blue areas are covered by waters during high tide, while they are unveiled by low tide. The speckle effect, that resembles salt and pepper is more apparent in the sea area, while land areas exhibit a lower variation in the values. In

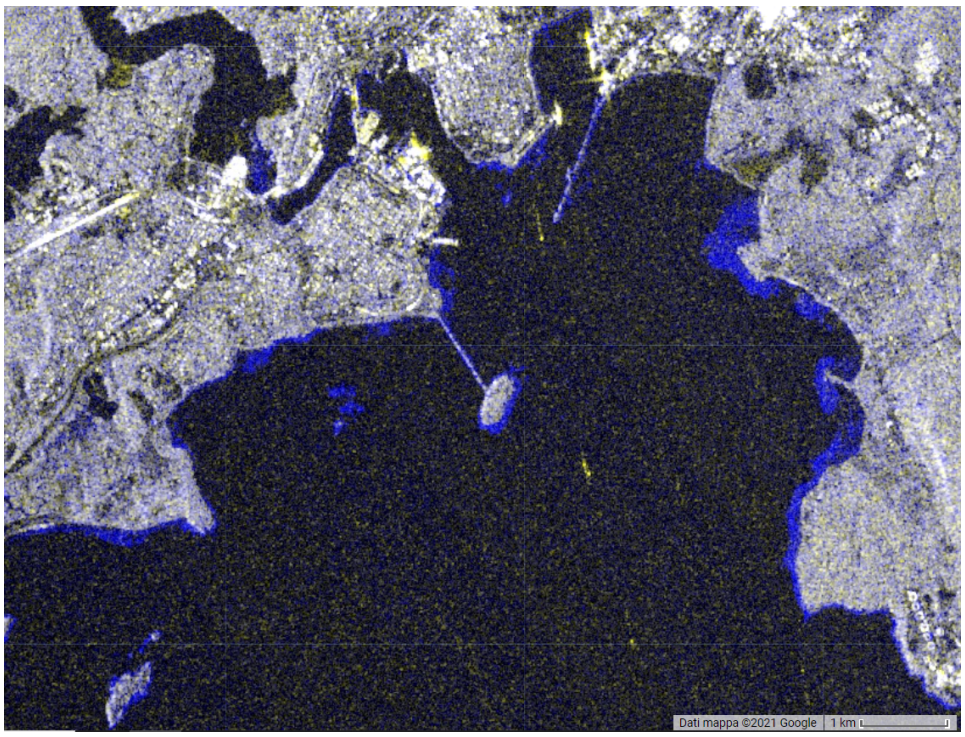

Figure 4.5: Composite image of the Saint John harbour area: yellow band with backscattering acquired during a high tide event, blue band with backscattering acquired during a low tide event.

Figure 4.5 some other elements are worth to describe. The yellow bright spots in the upper part of the figure, close to the harbor could be ships anchored at the port. Other spots that also are likely vessels are located in the middle of the gulf.

4.3.2 Single image coastline detection

Having identified this interesting area, the work went in the direction of exploiting the developed coastline detection method on single acquisitions of extreme – in the sense of very high or low – tides. In this way, we aimed at detecting precisely the tidal plains that are frequently inundated and uncovered by tides. It is worth noting that in the previous case of the Lizard Island the algorithm was applied on a temporally averaged scene that reduced the speckle problem. In this case we use the same images of the previous sub-

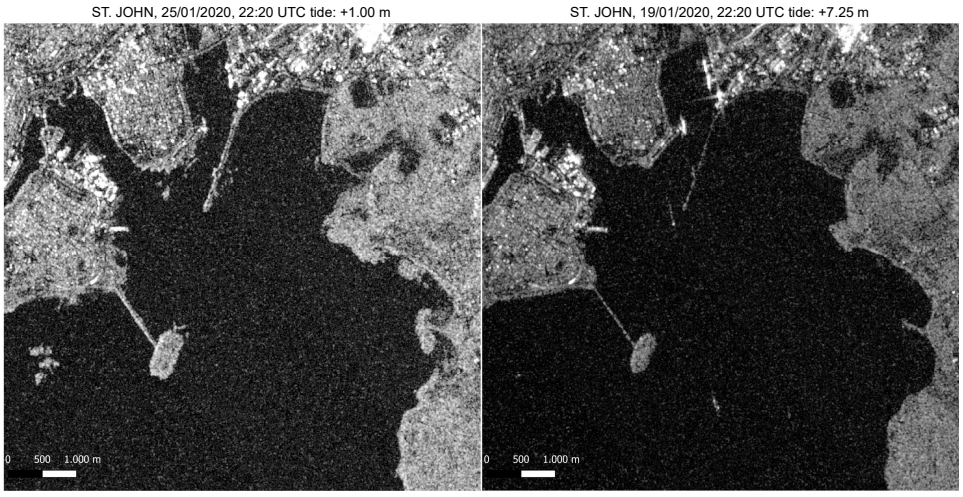

Figure 4.6: Two Sentinel-1 scenes with VH-polarization for the Fundy area, with high and low tide.

section, that are depicted in Figure 4.6. The proposed approach for the segmentation is the same adopted for the Lizard Island area. The number of iterations remains equal to two and, the thresholding algorithm chosen is Otsu's method. However, modifications in the parameters are adapted to fit the current area that has a higher detail in the coastline. Moreover, the detection is based on a single acquisition, hence speckle presents a larger variation in intensity. The obtained result presents some superpixels classified in the sea class that are in the real world tiny water bodies or even areas with low backscattering inside the land. To filter these small features the surface size is used as a discriminant. If the surface is less than a cer-

Parameter		High tide	Low tide
Segmentation 1	Superpixel size	200	400
	Compactness	2	2
Segmentation 2	Superpixel size	64	49
	Compactness	2.5	2.5
Minimum superpixel area	[m^2]	40000	40000

Table 4.1: Recap of the parameters settings for the coastline detection algorithm in the high and low tide single images. The last is the limit area for water regions inside a land area to be considered significant and be kept in the final result.

tain threshold then the border of the water area is erased. This operation highlights the main coastline and erases small features. Table 4.1 shows the most important parameters tuned to get the coastline shown in Figure 4.7.

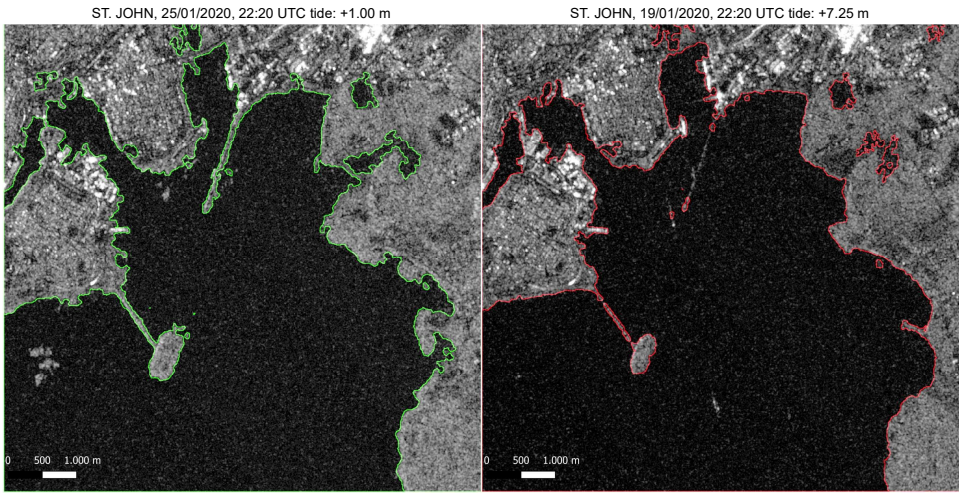

Figure 4.7: The coastline detection algorithm is applied to two Sentinel-1 scenes of VH-polarization for the Fundy area, with high and low tide.

The results of this segmentation demonstrate that the proposed approach is capable of detecting the coastline in more challenging situations. Urban areas have a distinctive high backscattering due to signal bouncing effects. Moreover, when a single image is the input of the algorithm, speckle has a larger variation than when multitemporal filters are adopted. However, this

approach can depict the high-level details of the harbor area. In the area, there are two human-made land-stripes that are the object of Figure 4.8. The left one is made of gravel and, despite the narrow size, approximately 20 m, can be detected by the process. On the right side, there is a wharf that leads to a lighthouse. This one is approximately 15 m wide but has a smooth surface. When the tide is high the approach cannot identify it as land. Another wrong classification of the model are the tiny islands on the left side

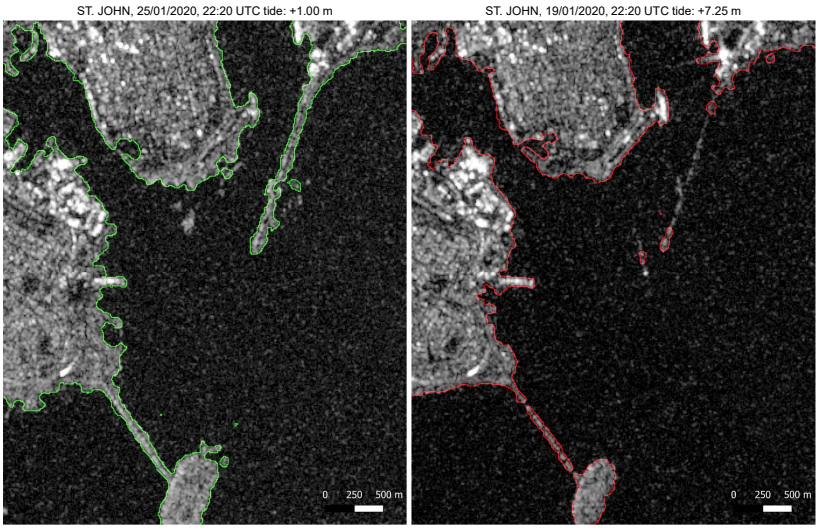

Figure 4.8: The coastline detection algorithm is applied to two Sentinel-1 scenes of VH-polarization for the Fundy area, with high and low tide. Here a zoom of the wharfs in the harbor is shown.

of the low tide image that the algorithm fails to detect. What happened is that this area is not classified in the sea cluster by the first iteration, because of the large superpixel size in the first segmentation compared to the island size. In the following subsection, after having described the dispersion index (DI), a comparison with the results of this analysis is carried out.

4.3.3 Dispersion index

The results presented in the previous subsection can highlight the differences between two single images acquired at two specific points in time. In this subsection, a more comprehensive approach is presented by analyzing a larger amount of data. The source mission is always Sentinel-1, and GEE is used for the processing. The time-series data consists of 60 VH-polarized scenes. The acquisition dates span from September 2019 to April 2020 (with satellites 1A and 1B). The dispersion index measures the stability over time of the

terrestrial surface. It was first introduced for detecting permanent scatterers in the context of InSAR in [Ferretti et al., 2001]. The statistics of mean and standard deviation (SD) are computed with all the values in the time series for that specific pixel. The dispersion index is obtained by dividing the mean by the standard deviation:

$$D_i = \frac{\mu_i}{\sigma_i}$$

The main idea behind this computation is to exploit the large dataset to spot areas that are alternatively covered by water thanks to their characteristic standard deviation. This hypothesis is confirmed by Figure 4.9, where the components for the computation are shown with the final result.

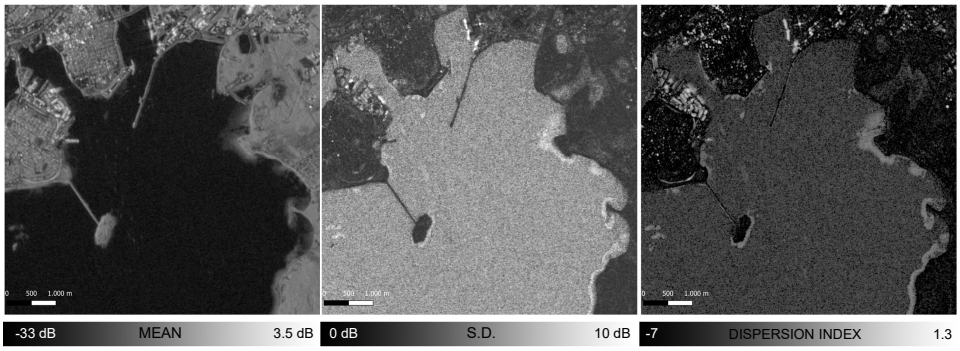

Figure 4.9: Statistics of a 60 acquisitions time-series: μ, σ, and Dispersion index maps of the Saint John harbor area.

It is worth noting that by averaging a large number of acquisitions there is a great improvement in the depiction of the urban area in the upper part of the left square. On the east side of the scene, it is already possible to individuate areas with an intermediate average value between stable land and stable sea. The central image depicts the SD of the time series. This metric exhibits low values for land areas that present backscattering stability in time. On the other end, sea pixels present a higher backscattering SD in time. This variability is due to the speckle effect and to the continuous modification of the sea surface due to varying wave height and direction. This part of the image confirms what we discussed in Chapter 3. Even higher values can be appreciated in the tidal plains, where the alternation of acquisitions that present land and sea make this area very variable. By checking the harbor area in the upper part of the map, it is possible to notice some elongated and bright spots. Those are docking sites for oil tankers that come and go. The standard deviation there is even higher than the tidal plain because, when present, the bouncing of the signal makes their backscattering very bright.

This is clearly visible in 4.10. It is interesting to see that despite the large denominator, being the numerator of small absolute value but negative, the spot is clearly visible also in the dispersion index image.

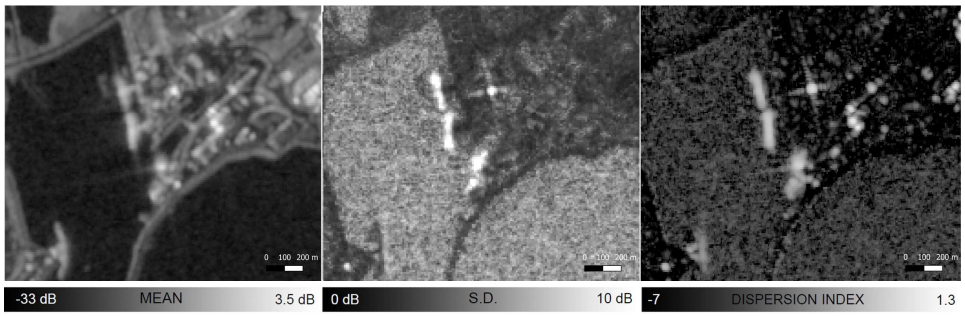

Figure 4.10: Statistics of a 60 acquisitions time-series: μ, σ, and Dispersion index maps of the Saint John harbor area. Zoom on the spot where oil tanker refill.

The square on the right in Figure 4.9 presents the map of the dispersion index. This representation has a high potential for the individuation of the tidal plains. Those areas present a distinctive higher value with respect to the very low stable land and sea pixel. This happens because, being the numerator values negative, the division with the large SD of these areas makes the result small in absolute value. On the other hand, stable sea and stable land, are divided by a small SD that make the result larger in absolute value. Urban and unstable areas (in the sense that change in amplitude occurs) are the only ones that present a higher DI than tidal plains.

Figure 4.11 compares the result of the previous subsection with the DI map. The region between the red line and green line (respectively the high and low tide coastlines) was covered by water on the first acquisition but was land in the second. The most visible portion is on the east side of the image. The DI map confirms the oscillation of the sea level in this region in the considered period. This demonstrates the proper choice of the two acquisitions. The most visible error is the lighthouse wharf on the upper part of the image. The DI map indicates it is constantly above water since it is as dark as stable land. In contrast, the red detection is not able to individuate it as land, probably because of the small width.

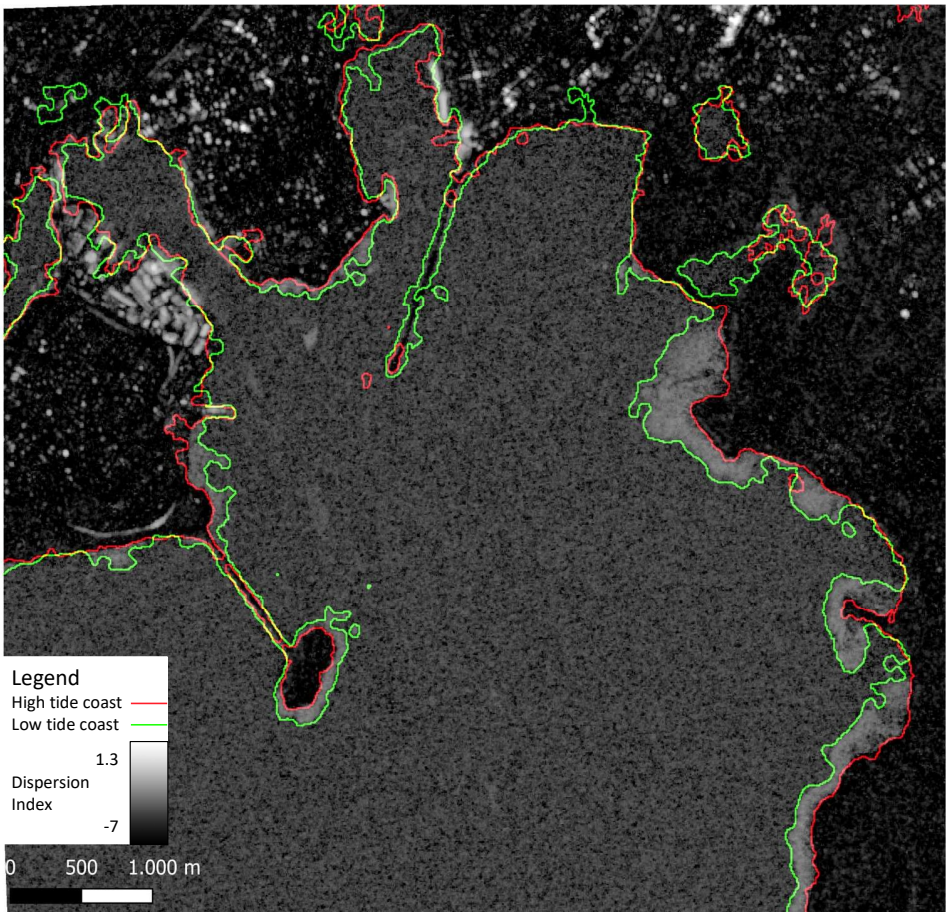

Figure 4.11: Comparison between coastal detection in two acquisition and use of long term statistics for tidal plain monitoring. The red and green lines are the detected coastlines for high and low tide events. Note that when the two lines overlap, the result becomes yellow. On the background there is the DI map.

4.4 Coastal monitoring: Reentrâncias Maranhenses

This subsection deals with the analysis of the results and the comparison with other techniques. Coastlines can present a dynamic that modifies their shape in just a few decades. It is the case of the natural protected area in Northern Brazil called Reentrâncias Maranhenses, close to the deltas of the Amazon and Tocantins rivers. Accretion and erosion phenomena are attributed to strong oceanic waves and tidal currents that can move large quantities of sand [Magris and Barreto, 2010], as Figure 4.12 depicts. This region is protected because it is the habitat of mangroves.

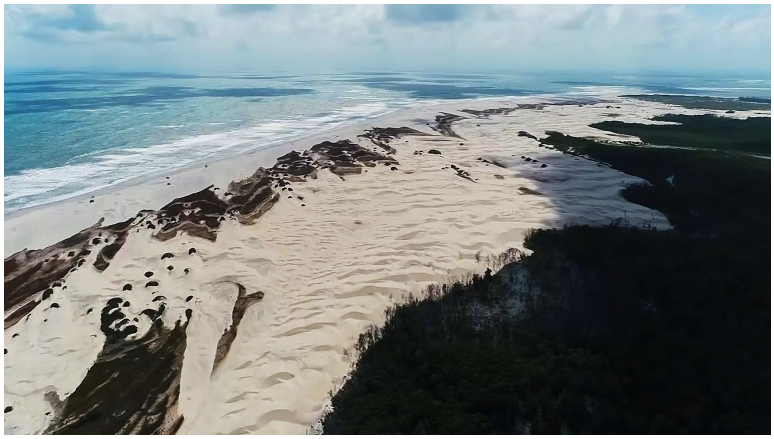

Figure 4.12: A typical sandy beach in the natural reserve of Reentrâncias Maranhenses.

4.4.1 Preliminary data analysis

The preliminary analysis is performed using a stack of scenes acquired over a period of three years. VH polarization channel are selected and grouped by year. Then, pixel values are averaged to reduce speckle, tidal effects and extreme events. Finally, GEE permits to compose an image with each year value in every band of the RGB codification. These trivial operations allow us to compare the coastline over many years; the changes are visible in Figure 4.13. This analysis cannot identify the exact change date for the

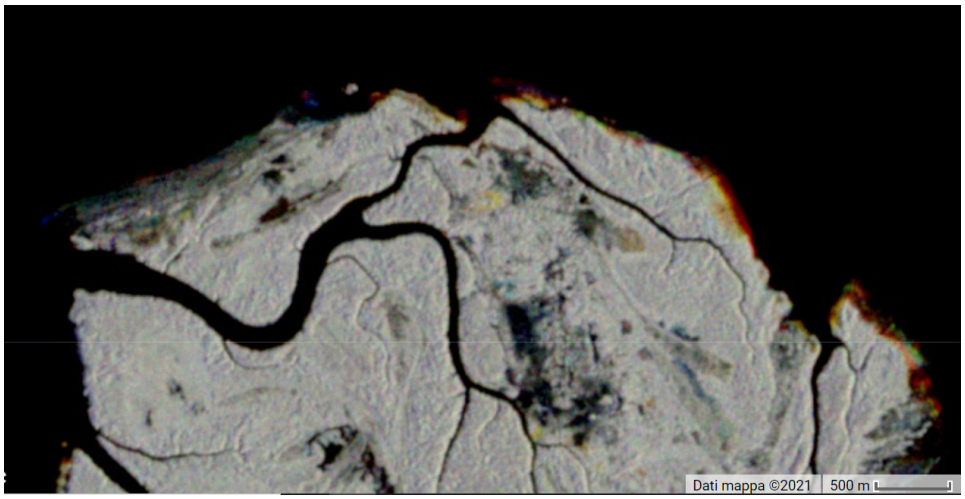

Figure 4.13: Composite image of the coastline in the Reentrâncias Maranhenses: red band with 2017 VH polarized band median, green band with 2018 polarized band median, blue band with 2020 polarized band median.

pixels, but only the year. Moreover, there are areas with complex behavior and a difficult interpretation on the left of the scene. Some information can be extracted from this map: there is a red-colored linear shore with direction N-W to S-E on the right part of the scene. It is possible to infer that the backscatter in this area was on average higher in the first year of the analysis. Hence, an erosion is taking place. Moreover, the vast area with a blue-green coloration on the left part of the scene hints that the coastline is expanding in that area. These information will be proven correct in the next pages. However, a deeper analysis is conducted to identify with better precision location and date-of-change of the morphological modification that are taking place in this area.

4.4.2 Results of the monitoring

In this subsection, we analyze the dynamics of accretion or erosion. The regions are identified thanks to the exploratory analysis. The data processing that leads to the following visualizations is described extensively in Section 3.3. Two coastal traits are explored to depict erosion and accretion phenomena.

Figure 4.14 depicts a large erosion that occurs for a coastal length of nearly 700 m. The depth of erosion (in direction perpendicular to the coastline) is around 70 m. The erosion is gradual: a slice of around 20 m is lost every year. This phenomenon can well be captured by the map on the left panel with the hue-based visualization of the change-date. The right panel depicts the behavior of the NLWI index over time and confirms the previous analysis.

All the points under scrutiny are selected on the interesting transect. Point D is on the coast in the first season, but gradually the NLWI decreases. The date of covering by water can be estimated thanks to the linear model. According to the proposed model, for point D the covering happens between Spring and Summer 2017. For point C the transformation to sea comes a little bit later as well as for point B. Point A is very close to the coastline at the time of the last acquisitions, but the general behavior makes it likely that the correct change-date is at the end of 2020. A very simple model was chosen to avoid over-fitting the very complex behavior of coastal traits that don't have a clear dynamic. In the following paragraph the comparison with optical data is carried out.

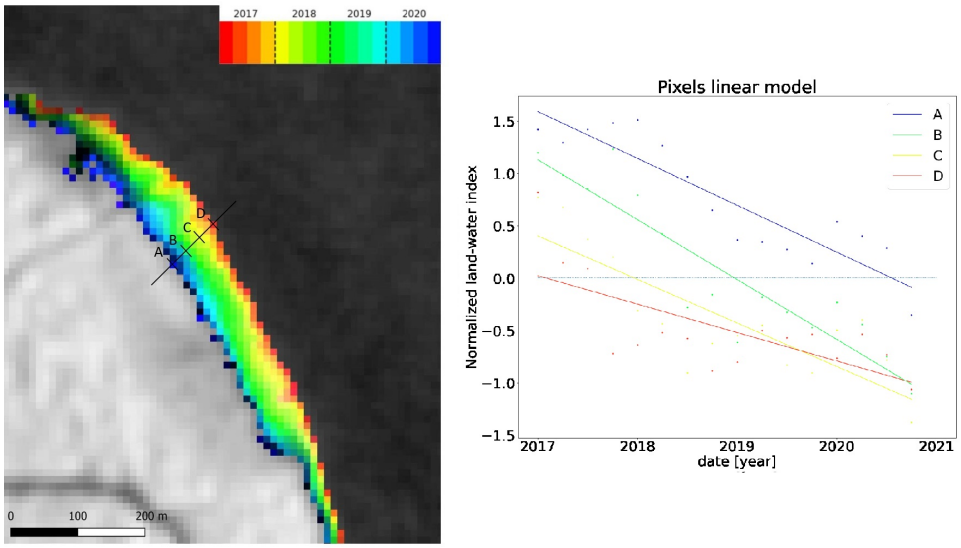

Figure 4.14: On the left: visualization of an eroded beach with the change-date used as hue. More details about the visualization can be found in Section 3.3. The background is the average r value for each pixel over the 4 years of analysis. On the right, the estimated model for the points A,B,C,D on the transect visible on the left image. The color of the data and the corresponding linear model correspond to the color of the pixel.

Comparison with optical

Optical remote sensing is described as not suitable for consistent monitoring in the introduction chapter. In this equatorial area, clouds often constitute an obstacle for the observation of the earth's surface. The search for cloud-free acquisitions focused on the first quarter of the year and it is here presented as a validation. Data are provided by the commercial company Planet. This company is selected because its wide data-set available. Their aim is to provide optical imagery with a high temporal and spatial resolution. Their products have a 3 m or 0.8 m resolution and, thanks to the 130 operating satellites, high temporal resolution. A part of their dataset is open to academic researchers and students. The access is limited to specific products and to 5,000 square kilometers of data per month.

Figure 4.15 depicts the eroded area presented in the previous pages in the analyzed years. Four optical acquisitions are compared. The search is focused on the first quarter of each year. The best image in that period

is chosen, but for the years 2017 and 2020, the best cloud-free image of the area was found only in late March. This demonstrates the difficulty to obtain consistent data when clouds are an important factor.

The four acquisitions do not present the same tidal height. However, the coastal position comparison with the graduated transect confirms the results of the SAR-based change-visualization. The vegetated area shrunk year by year, even if the behavior is more complex than what might be guessed from Figure 4.13. The disappearance date (according to the monitoring method) for the four investigated points is from outer to inner: 2^{nd} quarter of 2017, 4^{th} quarter of 2017, beginning of 2019, 3^{rd} quarter of 2020. It is worth noting

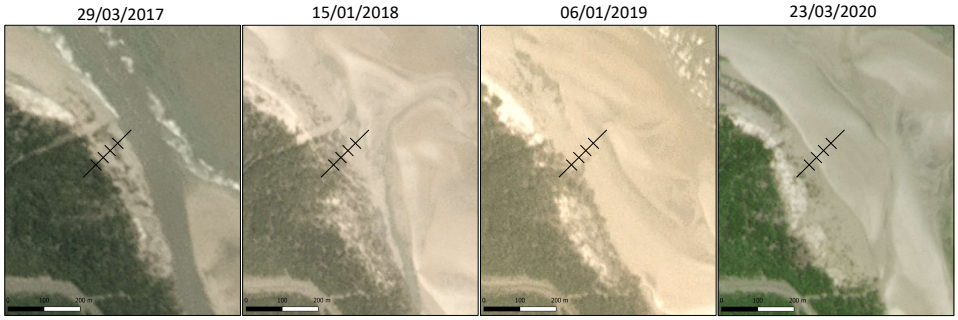

Figure 4.15: The optical acquisitions operated by ©Planet Labs Inc. Each acquisition shows the state of the coast for the area in each year, but tidal level could be different for each square. However, it is possible to appreciate the regression of the vegetated area. The black transect with the gridded bar is the same one that was on Figure 4.14, so that a comparison with the SAR analysis is possible.

that with optical imagery the delineation of the shoreline is not trivial in this context because of the similar color between dry sand, wet sand and shallow waters that is the object of the optical measurement systems. Moreover, it could be difficult to identify the coastlines if a vegetated area is inundated. In contrast, it is worth highlighting that SAR-based systems investigate a different physical parameter: the roughness of the interacting object. The surface might be smooth for both wet sand and shallow water, but for dry sand and vegetation, the roughness is substantially different. Hence also the backscattered signal presents more peculiarity that make the coastline detection easier. Besides that, the ability to acquire measurements consistently allows for temporal filtering that can erase the tidal effect that would influence negatively the long-term analysis.

In the previous paragraph, we focused on a trait of coast that presents a

gradual and slow behavior of erosion. On the same branch of the complex Daedalus of islands that form the Reentrâncias Maranhenses natural reserve lies the next area of interest. In this second case, the complex tide and marine currents sand transport phenomenon created an island very close to the coastline. This happened in a short period, between the end of 2018 and the beginning of 2020. Figure 4.16 shows this accretion process of the island where the graduated transect is placed. The details of this monitoring visualization technique are the same that we used in the previous pages and are explained in Section 3.3. What is important to remember is that each colored pixel has a hue defined according to the estimated date of appearance of land in the resolution cell. The new island has a size of around 10'000 m^2. The inner part in green and the outer edge is blue. The information that the visualization carries is that the appearance of this island happened not before 2018. This time-related information can be extrapolated just by looking at the map. A confirmation of this is presented in the bottom square, with the *NLWI* linear model for the four pixels that lie on the graduated transect. It is possible to note that the point named B, C and D have a very similar behavior with a steady increase in the *NLWI* index and an estimated land emergence between the 2^{nd} and 3^{rd} quarter of 2018. In contrast, in the point A resolution cell– which is located on the outer ring– land appears just from the autumn of 2019.

It is worth noting that the in the middle part of the image, there is a beach accretion phenomena. It is constant in time: the inner pixels appear at the beginning of 2017 and more outer pixels appear later, with the outer slice appeared in late 2020. However, the dark color indicates that the value (V for the HSV codification) for the pixel is low. This means that the average *NLWI* computed after the change is similar to 0, hence transformation to land pixel is not so clear. For this reason the pixel is darkened to depict an uncertainty in the detection. The low *NLWI* is likely due to the averaging over the season: it happens that in some images the area was covered by tide and in some not. The result is that the average r value for the season is close to the threshold, but still increasing over time.

The seasonal averaging is important for this reason: it is possible to get an insight on a long term phenomenon that comparison between single acquisitions could not depict because of the noise that is caused by instrumental limitations (the presence of speckle) but also by the tides (that make the behavior of a coastline oscillate in time).

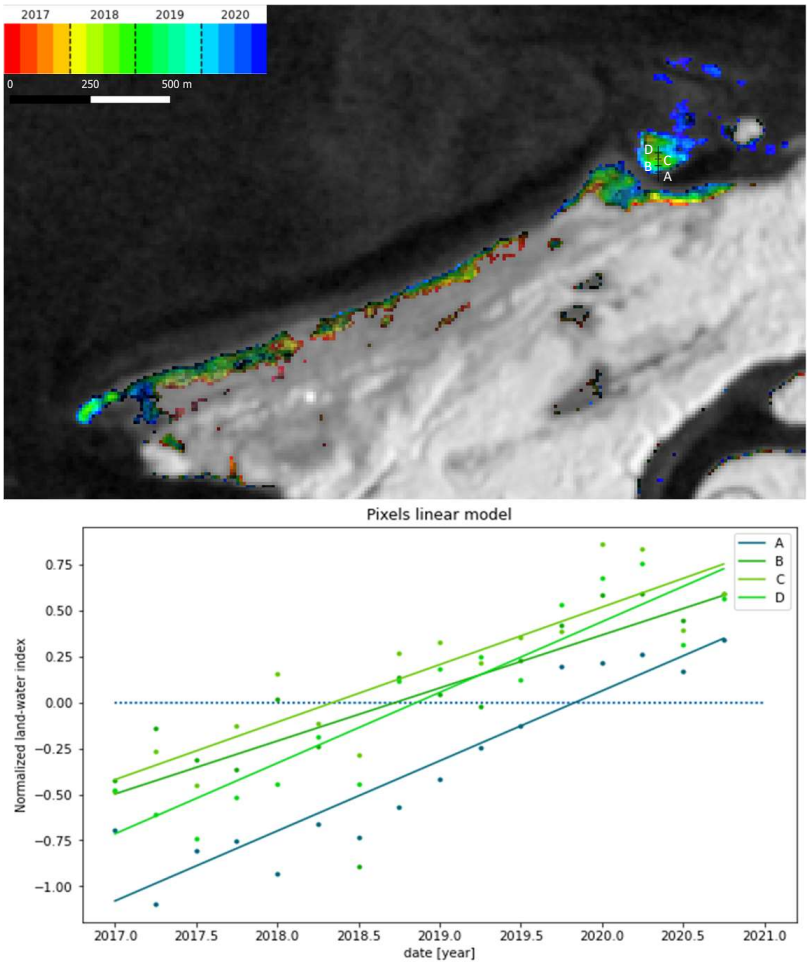

Figure 4.16: On the top panel: visualization of an accretion phenomenon with the change-date used as hue. More details about the visualization can be found in Section 3.3; on the background the average r value for each pixel over the 4 years of analysis. On the bottom panel: the estimated model for the points A,B,C,D on the transect visible on the top panel. The color of the data and the corresponding linear model matches the color of the pixel.

Comparison with deep learning algorithm

The results of the monitoring approach in the area are compared to the output of the algorithm for water detection described in [Asaro et al., 2021]. It exploits a U-Net deep learning architecture for water segmentation in SAR images. The training set consists of small patches of Sentinel-1 acquisitions over the Low Countries (Netherlands, Belgium). However, this algorithm demonstrates to works well also in other settings like the studied natural

area of the Reentrâncias Maranhenses.

Figure 4.17 depicts the results of this algorithm on the same area that was analyzed with the monitoring technique with, in the background the average backscattering for the monitored period. The island with the graduated transect is not detected in the acquisitions on 01/03/2017 and 07/02/2019 but is detected on 26/02/2020. This would suggest the estimation of the monitoring method might be anticipated with respect to the actual time of appearance. However, the problem of oscillating sea level makes the validation hard and there are chances the single scene of 2019 the algorithm is based on was acquired during high tide.

In the middle part of the scene, there seems to have been a forward movement of the beach starting from after the first detection. This result agrees with the information carried by Figure 4.16. In contrast, the tiny island located on the far left side could not be detected by the algorithms, while the monitoring model was able to depict his appearance in the second half of the analyzed period.

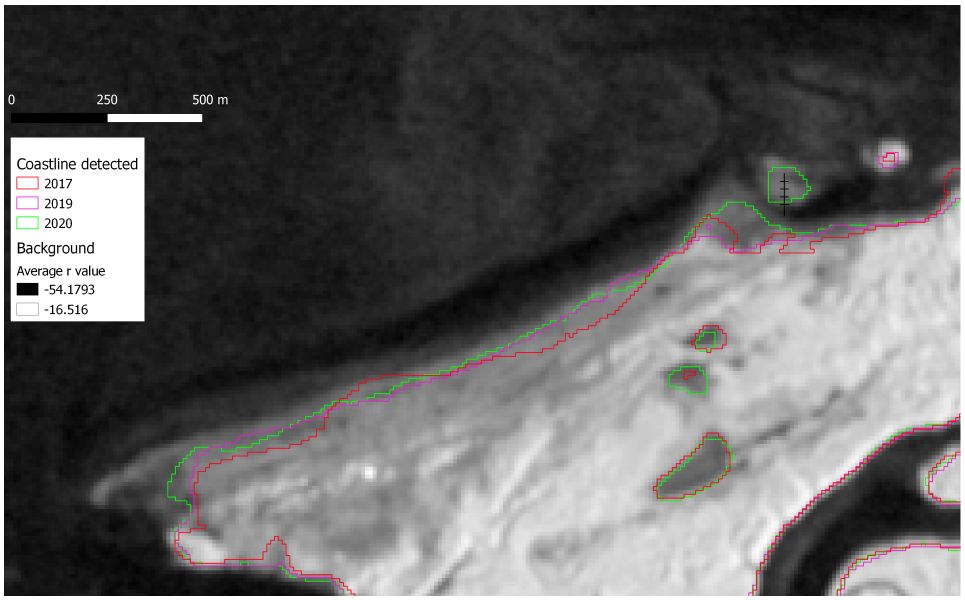

Figure 4.17: The detected coastline with the algorithm from [Asaro et al., 2021] on a single SAR scenes acquired on the 01/03/2017, 07/02/2019, 26/02/2020. On the background the average r value for each pixel over the 4 years of analysis. The black graduated transect allows the comparison with the previous Figure.

It is worth highlighting that the deep learning approach works on single SLC acquisitions, hence suffers from the issue of varying tides when comparing scenes. The output of this algorithm might be correct in identifying the

coastline for this specific image however, coastlines oscillate continuously for the tidal variation. Hence the snapshot of a coastline is not as informative as the identification of the long-term trend for the problem of monitoring.

Chapter 5

Conclusions

This thesis' objective was to design and develop novel approaches in the field of coastline detection and monitoring. The technology adopted is SAR-remote sensing and is chosen for its advantages of all-weather, day-and-night and constant illumination over optical systems.

Coastal detection is tackled in literature with a variety of methods that span from simple pixel processing to deep learning. The approach that this thesis proposes can be described as an unsupervised approach, taking the definition from the machine learning field. A new iterative coastline detection algorithm has been developed with the adoption of processes related to image segmentation– like SLIC– and statistical analysis, like the Gaussian mixtures model or Otsu's method. The validation is carried out by comparing the method's results over the Lizard Island with a manually detected shore with optical imagery. The average distance is 12 m and 80% of the two coastlines are separated by less than 20 m. An estimation with a precision higher than half of the resolution is out of reach for this kind of approach. Future developments could look in the direction of classifying superpixels based on multiple features such as both the polarizations, the statistics of the superpixels and also multi-temporal attributes.

We propose an innovative approach for monitoring that exploits the consistent acquisitions of the Sentinel-1 mission. A long-term data-set allows erasing the tidal level variation by averaging on a seasonal basis. Moreover, the proposed NLWI index overcomes issues in comparing images with different sea-states, which would be problematic. The map visualization of the change-date –estimated through a linear model of NLWI with time– proved to be an effective information carrier. Future developments include the validation with ground truth data and the adoption of a more complex NLWI-time model to describe different dynamics.

Bibliography

[Achanta et al., 2010] Achanta, R., Shaji, A., Smith, K., Lucchi, A., Fua, P., and Susstrunk, S. (2010). Slic superpixels. *Technical report, EPFL*.

[Asaro et al., 2021] Asaro, F., Murdaca, G., and Prati, C. M. (2021). Learning deep models from weak labels for water surface segmentation in sar images. In *IGARSS 2021-2021 IEEE International Geoscience and Remote Sensing Symposium*. IEEE.

[Baselice and Ferraioli, 2013] Baselice, F. and Ferraioli, G. (2013). Unsupervised coastal line extraction from sar images. *IEEE Geoscience and Remote Sensing Letters*, 10(6):1350–1354.

[Bruno et al., 2019] Bruno, M. F., Molfetta, M. G., Pratola, L., Mossa, M., Nutricato, R., Morea, A., Nitti, D. O., and Chiaradia, M. T. (2019). A combined approach of field data and earth observation for coastal risk assessment. *Sensors*, 19(6).

[Demir et al., 2017] Demir, N., Oy, S., Erdem, F., Şeker, D. Z., and Bayram, B. (2017). Integrated shoreline extraction approach with use of rasat ms and sentinel-1a sar images. *ISPRS Annals of Photogrammetry, Remote Sensing and Spatial Information Sciences*, IV-2/W4:445–449.

[Dolan et al., 1991] Dolan, R., Fenster, M. S., and Holme, S. J. (1991). Temporal analysis of shoreline recession and accretion. *Journal of Coastal Research*, 7(3):723–744.

[Ferreira et al., 2006] Ferreira, O., Garcia, T., Matias, A., Taborda, R., and Dias, J. (2006). An integrated method for the determination of set-back lines for coastal erosion hazards on sandy shores. *Continental Shelf Research*, 26:1030–1044.

[Ferrentino et al., 2020] Ferrentino, E., Nunziata, F., Buono, A., Urciuoli, A., and Migliaccio, M. (2020). Multipolarization time series of sentinel-1

sar imagery to analyze variations of reservoirs' water body. *IEEE Journal of Selected Topics in Applied Earth Observations and Remote Sensing*, 13:840–846.

[Ferretti et al., 2001] Ferretti, A., Prati, C., and Rocca, F. (2001). Permanent scatterers in sar interferometry. *IEEE Transactions on Geoscience and Remote Sensing*, 39(1):8–20.

[Fletcher and ESA, 2012] Fletcher, K. and ESA (2012). *Sentinel-1: ESA's Radar Observatory Mission for GMES Operational Services*. ESA SP. ESA Communications.

[Garcia-Rubio et al., 2015] Garcia-Rubio, G., Huntley, D., and Russell, P. (2015). Evaluating shoreline identification using optical satellite images. *Marine Geology*, 359:96–105.

[Gomes et al., 2020] Gomes, V. C. F., Queiroz, G. R., and Ferreira, K. R. (2020). An overview of platforms for big earth observation data management and analysis. *Remote Sensing*, 12(8).

[Gorelick et al., 2017] Gorelick, N., Hancher, M., Dixon, M., Ilyushchenko, S., Thau, D., and Moore, R. (2017). Google earth engine: Planetary-scale geospatial analysis for everyone. *Remote Sensing of Environment*, 202:18–27. Big Remotely Sensed Data: tools, applications and experiences.

[IPCC, 1990] IPCC (1990). *Policymakers' Summary of the Potential Impacts of Climate Change: Report from Working Group II to IPCC*. Department of the Arts, Sport, the Environment, Tourism, and Territories.

[Magris and Barreto, 2010] Magris, R. A. and Barreto, R. (2010). Mapping and assessment of protection of mangrove habitats in brazil. *Pan-American Journal of Aquatic Sciences*, 5.

[Martinez et al., 2007] Martinez, M., Intralawan, A., Vázquez, G., Pérez-Maqueo, O., Sutton, P., and Landgrave, R. (2007). The coasts of our world: Ecological, economic and social importance. *Ecological Economics*, 63(2):254–272. Ecological Economics of Coastal Disasters.

[Mentaschi et al., 2018] Mentaschi, L., Vousdoukas, M., and Pekel, J. e. a. (2018). Global long-term observations of coastal erosion and accretion. *Scientific Reports*, 8(1).

[Moreira et al., 2013] Moreira, A., Prats-Iraola, P., Younis, M., Krieger, G., Hajnsek, I., and Papathanassiou, K. P. (2013). A tutorial on synthetic

aperture radar. *IEEE Geoscience and Remote Sensing Magazine*, 1(1):6–43.

[Mouche et al., 2006] Mouche, A. A., Hauser, D., and Kudryavtsev, V. (2006). Radar scattering of the ocean surface and sea-roughness properties: A combined analysis from dual-polarizations airborne radar observations and models in c band. *Journal of Geophysical Research: Oceans*, 111(C9).

[Muller et al., 2010] Muller, M., Bernard, L., and Brauner, J. (2010). Moving code in spatial data infrastructures - web service based deployment of geoprocessing algorithms. *Transactions in GIS*, 14(s1):101–118.

[Oliver and Quegan, 1998] Oliver, C. and Quegan, S. (1998). *Understanding Synthetic Aperture Radar Images*. Raleigh.

[Otsu, 1979] Otsu, N. (1979). A threshold selection method from gray-level histograms. *IEEE Transactions on Systems, Man, and Cybernetics*, 9(1):62–66.

[Paek et al., 2020] Paek, S. W., Balasubramanian, S., Kim, S., and de Weck, O. (2020). Small-satellite synthetic aperture radar for continuous global biospheric monitoring: A review. *Remote Sensing*, 12(16).

[Soille et al., 2018] Soille, P., Burger, A., De Marchi, D., Kempeneers, P., Rodriguez, D., Syrris, V., and Vasilev, V. (2018). A versatile data-intensive computing platform for information retrieval from big geospatial data. *Future Generation Computer Systems*, 81:30–40.

[Spinosa et al., 2018] Spinosa, A., Ziemba, A., Saponieri, A., Navarro-Sanchez, V. D., Damiani, L., and Serafy, G. E. (2018). Automatic extraction of shoreline from satellite images: a new approach. In *2018 IEEE International Workshop on Metrology for the Sea; Learning to Measure Sea Health Parameters (MetroSea)*, pages 33–38.

[Stive et al., 2002] Stive, M. J., Aarninkhof, S. G., Hamm, L., Hanson, H., Larson, M., Wijnberg, K. M., Nicholls, R. J., and Capobianco, M. (2002). Variability of shore and shoreline evolution. *Coastal Engineering*, 47(2):211–235. Shore Nourishment in Europe.

[Tajima et al., 2019] Tajima, Y., Wu, L., Fuse, T., Shimozono, T., and Sato, S. (2019). Study on shoreline monitoring system based on satellite sar imagery. *Coastal Engineering Journal*, 61(3):401–421.

[Tanaka et al., 2012] Tanaka, A., Uehara, K., Tamura, T., and Saito, Y. (2012). Area change detection in river mouthbars at the mekong river delta using synthetic aperture radar (sar) data. In *2012 IEEE International Geoscience and Remote Sensing Symposium*, pages 4911–4914.

[Teodoro, 2016] Teodoro, A. (2016). *Optical Satellite Remote Sensing of the Coastal Zone Environment – An Overview*. Maged Marghany.

[Toure et al., 2019] Toure, S., Diop, O., Kpalma, K., and Maiga, A. S. (2019). Shoreline detection using optical remote sensing: A review. *ISPRS International Journal of Geo-Information*, 8(2).

[Turner et al., 1998] Turner, R. K., NeilAdger, W., and Lorenzoni, I. (1998). Towards integrated modelling and analysis in coastal zones: Principles and practices. *LOICZ REPORTS & STUDIES NO. 11*.

[Urciuoli et al., 2019] Urciuoli, A., Buono, A., Nunziata, F., and Migliaccio, M. (2019). Analysis of local-and non-local filters for multi-polarization sar coastline extraction applications. In *2019 IEEE 5th International forum on Research and Technology for Society and Industry (RTSI)*, pages 28–33.

[Wei et al., 2021] Wei, X., Zheng, W., Xi, C., and Shang, S. (2021). Shoreline extraction in sar image based on advanced geometric active contour model. *Remote Sensing*, 13(4).